

¹ A novel inf–sup–based volumetric constraint ratio and
² its implementation via mixed FE-meshfree formulation

³ Junchao Wu^{a,*}, Yingjie Chu^b, Yangtao Xu^a

^a Key Laboratory for Intelligent Infrastructure and Monitoring of Fujian Province, College
of Civil Engineering, Huaqiao University , Xiamen, Fujian, 361021, China

^b Fujian Key Laboratory of Digital Simulations for Coastal Civil Engineering, Department
of Civil Engineering, Xiamen University , Xiamen, Fujian, 361005, China

⁴ **Abstract**

Numerical formulations for incompressible materials often suffer from volumetric locking, which reduces the accuracy of displacement solutions and introduces oscillations in the pressure field. A well-chosen constraint ratio can mitigate this issue, but traditional approaches lack a theoretical foundation based on the inf–sup (or LBB) condition, which is essential for the stability of mixed formulations. This paper introduces a novel optimal constraint ratio derived from the inf–sup condition to address volumetric locking. The inf–sup test, a numerical tool for verifying the inf–sup condition, is reaffirmed to be equivalent to the inf–sup condition through a variational approach. By incorporating a complete polynomial space whose dimension matches the number of displacement degrees of freedom (DOFs), a new inf–sup value estimator is developed, explicitly considering the constraint ratio. For a given number of displacement DOFs, when the pressure DOFs of a numerical formulation remain below a stabilized number that falls into the optimal constraint ratio range, this numerical formulation actually satisfies the inf–sup condition. To implement the optimal constraint ratio, a mixed finite element and meshfree formulation is proposed, where displacements are discretized using traditional finite element approximations, and pressures are approximated via the reproducing kernel meshfree method. Leveraging the globally smooth reproducing kernel shape functions, the constraint ratio can be flexibly adjusted to meet the inf–sup condition without the limit of element. For computational efficiency and ease of implementation, pressure nodes are placed on selected displacement nodes to maintain the optimal constraint ratio. Inf–sup tests and a series of 2D and 3D incompressible elasticity examples validate the proposed constraint ratio, demonstrating its effectiveness in eliminating volumetric locking and enhancing the performance of mixed finite element and meshfree formulations.

⁵ **Keywords:** Optimal constraint ratio, Inf–sup condition estimator, Volumetric
⁶ locking, Mixed formulation, Reproducing kernel meshfree approximation

*Corresponding author

Email address: jcwu@hqu.edu.cn (Junchao Wu)

7 **1. Introduction**

8 The volumetric constraint is a necessary condition in the numerical formulation
 9 of incompressible materials like rubber and hydrogel. Proper imposition of
 10 this constraint is crucial for obtaining better numerical solutions; insufficient or
 11 excessive constraints will reduce the accuracy and stability of the solution [1].
 12 The volumetric constraint ratio [2], denoted as r , is often used to measure the
 13 level of constraint. It is defined as the total degrees of freedom (DOFs) of dis-
 14 placement divided by the total DOFs of pressure. Ideally, the optimal constraint
 15 ratio should be consistent with its governing partial differential equations. For
 16 example, in the two-dimensional (2D) case, the optimal constraint ratio is 2,
 17 since there are two governing equations for displacement and one for pressure.
 18 When the constraint ratio is less than 2, the formulation suffers from volumetric
 19 locking, while a constraint ratio greater than 2 can cause a coarse solution for
 20 pressure. These observations have been summarized as follows[2]:

$$r = \frac{2n_u}{n_p}, \quad \begin{cases} r > 2 & \text{too few constraints} \\ r = 2 & \text{optimal} \\ r < 2 & \text{too many constraints} \\ r \leq 1 & \text{severe locking} \end{cases} \quad (1)$$

21 where n_u and n_p are the numbers of control nodes for displacement and pressure,
 22 respectively. Classifying the locked status via the constraint ratio is straight-
 23 forward but imprecise. For instance, the constraint ratio can remain 2 while
 24 the pressure is discretized using continuous shape functions identical to the
 25 displacement's approximation. However, volumetric locking still exists in this
 26 formulation [2].

27 The inf-sup condition, also known as the Ladyzhenskay–Babuka–Brezzi
 28 (LBB) condition [3, 4], is a more precise requirement for a locking-free for-
 29 mulation. This condition is based on the mixed formulation framework, and
 30 when the inf-sup condition is satisfied, both the accuracy and stability of the
 31 mixed-formulation can be ensured. However, verifying the inf-sup condition is
 32 non-trivial. An eigenvalue problem namely inf-sup test can be used to check
 33 this condition numerically [5, 6, 7, 8]. Analytically, Brezzi and Fortin proposed
 34 a two-level projection framework that always satisfies the inf-sup condition, al-
 35 lowing it to be checked by identifying whether the formulation is included in
 36 this framework. Both analytical and numerical methods to check the inf-sup
 37 condition are complex, and the relationship between the constraint ratio and
 38 the inf-sup condition remains unclear.

39 To address volumetric constraint issues, adjusting the constraint ratio to an
 40 appropriate level is commonly used and easily implemented. In traditional finite
 41 element methods (FEM), this adjustment is carried out based on elements since
 42 the DOFs are embedded in each element. Conventional FEM often exhibits
 43 an over-constrained status. Reducing the approximation order of pressure in
 44 mixed formulation can alleviate the constraint burden, such as with the well-
 45 known Q4P1 (4-node quadrilateral displacement element with 1-node piecewise

constant pressure element) and Q8P3. Globally, using continuous shape functions to link the local pressure DOFs in each element can also reduce the total number of pressure DOFs and increase the constraint ratio, such as with T6C3 (6-node triangular displacement element with 3-node continuous linear pressure element) and Q9C4 (Taylor–Hood element) [9]. These schemes belong to the mixed formulation framework and can also be implemented through a projection approach, where the pressure approximant is projected into a lower-dimensional space. Examples include selective integration methods [10, 11], B–bar or F–bar methods [12, 13, 14, 15], pressure projection methods [16, 17, 18, 19, 20], and enhanced strain method [21]. Meanwhile, conventional 3-node triangular elements arranged in a regular cross pattern can also reduce the dimension of the pressure space [22]. It should be noted that not all of these methods meet the inf–sup condition despite alleviating volumetric locking and producing a good displacement solution. Some methods, like Q4P1, show significant oscillation for the pressure solution, known as spurious pressure mode or checkerboard mode [22]. In such cases, additional stabilization approaches, such as variational multi-scale stabilization (VMS) [23, 24, 25, 26, 27], Galerkin/least-squares (GLS) [28], or Streamline upwind/Petrov–Galerkin formulation (SUPG) [29, 30] are required to eliminate the oscillations in pressure.

Another class of FEM methods adjusts the constraint ratio by increasing the displacement DOFs. For instance, based on 3-node triangular elements, Arnold et al. [31, 32] used a cubic bubble function in each element to increase the displacement DOFs, known as the MINI element. It has been shown that this method belongs to the VMS framework [33], and its fulfillment of the inf–sup condition can be analytically evidenced using the two-level projection framework [7]. The Crouzeix–Raviart element [34] transfers the DOFs from the triangular vertices to edges, increasing the constraint ratio since, for triangular topology, the number of edges is greater than that of vertices. More details about FEM technology for volumetric constraint issues can be found in Refs. [2, 4, 35].

In the past two decades, various novel approximations equipped with globally smooth shape functions, such as moving least-squares approximation [36], reproducing kernel approximation [37, 38], radial basis functions [39, 40], maximum-entropy approximation [41], and NURBS approximation [42, 43], have been proposed. In these approaches, the approximant pressure evaluated by the derivatives of globally continuous shape functions also maintains a constraint ratio of 2 in 2D incompressible elasticity problems. However, the corresponding results still show lower accuracy caused by locking [44, 45]. Widely-used locking-free technologies for FEM are introduced in these approaches to enhance their performance. For example, Moutsanidis et al. [46, 47] employed selective integration and B–bar, F–bar methods for reproducing kernel particle methods. Wang et al. [48] applied selective integration schemes with bubble-stabilized functions to node-based smoothed particle FEM. Elguedj et al. [49] proposed the B–bar and F–bar NURBS formulations for linear and nonlinear incompressible elasticity. Chen et al. [50] adopted the pressure projection approach for reproducing kernel formulations for nearly-incompressible problems, which was later extended

to Stokes flow formulations by Goh et al. [51]. Bombarde et al. [52] developed a block-wise NURBS formulation for shell structures, eliminating locking via pressure projection. Casquero and Golestanian [53] proposed a NURBS-based continuous-assumed-strain element to alleviate volumetric locking. Most of these approximations offer better flexibility for arranging DOFs since their shape function constructions are no longer element-dependent. Huerta et al.[54] proposed a reproducing kernel approximation with divergence-free basis functions to avoid volumetric strain entirely , although this approach is unsuitable for compressible cases. Wu et al. [55] added extra displacement DOFs in FEM elements to resolve the locking issue, constructing local shape functions using generalized meshfree interpolation to maintain consistency. Vu-Huu et al. [56] employed different-order polygonal finite element shape functions to approximate displacement and pressure, embedding a bubble function in each element for stabilization.

This work proposes a more precise optimal volumetric constraint ratio and implements a locking-free mixed FE-meshfree formulation with this optimal constraint ratio. Firstly, the inf-sup condition is derived in a new form, showing that the inf-sup value equals to the lowest non-zero eigenvalue of dilatation stiffness in the context of variational analysis. Subsequently, involving a complete polynomial space with dimensions identical to displacement DOFs, the number of non-zero eigenvalues can be analytically calculated, and a new estimator considering the constraint ratio is established. From this estimator, the optimal constraint ratio is defined with a stabilized number of pressure nodes. If the constraint ratio exceeds the locking ratio, the formulation will show severe locking. When the constraint ratio is lower than the optimal ratio, the formulation achieves satisfactory results, and the inf-sup condition is fulfilled. This estimator provides a strong link between the inf-sup value and the pressure DOFs, making it possible to justify the locking status by counting the pressure nodes. Furthermore, a mixed FE-meshfree formulation is proposed to verify the optimal constraint ratio. In this mixed formulation, the displacement is approximated by traditional finite element methods, and the pressure is discretized by reproducing kernel meshfree approximation. With the aid of global RK shape functions, the pressure's DOFs can be adjusted arbitrarily without considering approximation order and numerical integration issues to maintaining the constraint ratio as optimal.

The remainder of this paper is organized as follows: Section 2 reviews the mixed formulation framework for incompressible elasticity problems. In Section 3, a novel estimator of the inf-sup value is developed, from which the optimal constraint ratio is obtained. Section 4 introduces the mixed FE-meshfree formulation and its corresponding nodal distribution schemes. Section 5 verifies the proposed optimal constraint ratio using a set of benchmark incompressible elasticity examples, studying error convergence and stability property for the mixed FE-meshfree approximation. Finally, the conclusions are presented in Section 6.

¹³⁶ **2. Mixed-formulation**

¹³⁷ *2.1. Nearly-incompressible elasticity*

¹³⁸ Consider a body $\Omega \in \mathbb{R}^{n_d}$ with boundary Γ in n_d -dimension, where Γ_t and
¹³⁹ Γ_g denote its natural boundary and essential boundary, respectively, such that
¹⁴⁰ $\Gamma_t \cup \Gamma_g = \Gamma$, $\Gamma_t \cap \Gamma_g = \emptyset$. The corresponding governing equations for the mixed
¹⁴¹ formulation are given by:

$$\begin{cases} \nabla \cdot \boldsymbol{\sigma} + \mathbf{b} = \mathbf{0} & \text{in } \Omega \\ \frac{p}{\kappa} + \nabla \cdot \mathbf{u} = 0 & \text{in } \Omega \\ \boldsymbol{\sigma} \cdot \mathbf{n} = \mathbf{t} & \text{on } \Gamma_t \\ \mathbf{u} = \mathbf{g} & \text{on } \Gamma_g \end{cases} \quad (2)$$

¹⁴² where \mathbf{b} denotes the prescribed body force in Ω . \mathbf{t}, \mathbf{g} are prescribed traction and
¹⁴³ displacement on natural and essential boundaries, respectively. \mathbf{u} and p , standing
¹⁴⁴ for displacement and hydrostatic pressure, respectively, are the variables of
¹⁴⁵ this problem. ∇ is the gradient tensor defined by $\nabla = \frac{\partial}{\partial x_i} \mathbf{e}_i$. $\boldsymbol{\sigma}$ denotes the
¹⁴⁶ stress tensor and has the following form:

$$\boldsymbol{\sigma}(\mathbf{u}, p) = p \mathbf{1} + 2\mu \nabla^d \mathbf{u} \quad (3)$$

¹⁴⁷ in which $\mathbf{1} = \delta_{ij} \mathbf{e}_i \otimes \mathbf{e}_j$ is the second-order identity tensor. $\nabla^d \mathbf{u}$ is the deviatoric
¹⁴⁸ gradient of \mathbf{u} and can be evaluated by:

$$\nabla^d \mathbf{u} = \frac{1}{2} (\mathbf{u} \nabla + \nabla \mathbf{u}) - \left(\frac{1}{3} \nabla \cdot \mathbf{u} \right) \mathbf{1} \quad (4)$$

¹⁴⁹ and κ, μ are the bulk modulus and shear modulus, respectively, and they can
¹⁵⁰ be represented by Young's modulus E and Poisson's ratio ν :

$$\kappa = \frac{E}{2(1-2\nu)}, \quad \mu = \frac{E}{3(1+\nu)} \quad (5)$$

¹⁵¹ In accordance with the Galerkin formulation, the weak form can be given
¹⁵² by: Find $\mathbf{u} \in V, p \in Q$, such that

$$\begin{cases} a(\mathbf{v}, \mathbf{u}) + b(\mathbf{v}, p) = f(\mathbf{v}) & \forall \mathbf{v} \in V \\ b(\mathbf{u}, q) + c(q, p) = 0 & \forall q \in Q \end{cases} \quad (6)$$

¹⁵³ with the spaces V, Q defined by:

$$V = \{ \mathbf{v} \in H^1(\Omega)^2 \mid \mathbf{v} = \mathbf{g}, \text{ on } \Gamma_g \} \quad (7)$$

¹⁵⁴

$$Q = \{ q \in L^2(\Omega) \mid \int_{\Omega} q \, d\Omega = 0 \} \quad (8)$$

155 where $a : V \times V \rightarrow \mathbb{R}$, $b : V \times Q \rightarrow \mathbb{R}$ and $c : Q \times Q \rightarrow \mathbb{R}$ are bilinear forms,
156 and $f : V \rightarrow \mathbb{R}$ is the linear form. In elasticity problems, they are given by:

$$a(\mathbf{v}, \mathbf{u}) = \int_{\Omega} \nabla^d \mathbf{v} : \nabla^d \mathbf{u} d\Omega \quad (9)$$

$$b(\mathbf{v}, q) = \int_{\Omega} \nabla \cdot \mathbf{v} q d\Omega \quad (10)$$

$$c(q, p) = - \int_{\Omega} \frac{1}{3\kappa} q p d\Omega \quad (11)$$

$$f(\mathbf{v}) = \int_{\Gamma_t} \mathbf{v} \cdot \mathbf{t} d\Gamma + \int_{\Omega} \mathbf{v} \cdot \mathbf{b} d\Omega \quad (12)$$

157 2.2. Ritz–Galerkin problem and volumetric locking

158 In the mixed-formulation framework, the displacement and pressure can be
159 discretized by different approximations. The approximant displacement \mathbf{u}_h and
160 approximant pressure p_h can be expressed by:

$$\mathbf{u}_h(\mathbf{x}) = \sum_{I=1}^{n_u} N_I(\mathbf{x}) \mathbf{u}_I, \quad p_h(\mathbf{x}) = \sum_{K=1}^{n_p} \Psi_K(\mathbf{x}) p_K \quad (13)$$

161 leading these approximations into the weak form of Eq. (6) yields the following
162 Ritz–Galerkin problems: Find $\mathbf{u}_h \in V_h$, $p_h \in Q_h$, such that

$$\begin{cases} a(\mathbf{v}_h, \mathbf{u}_h) + b(\mathbf{v}_h, p_h) = f(\mathbf{v}_h) & \forall \mathbf{v}_h \in V_h \\ b(\mathbf{u}_h, q_h) + c(q_h, p_h) = 0 & \forall q_h \in Q_h \end{cases} \quad (14)$$

163 For nearly incompressible material, the Poisson ratio approaches 0.5, and
164 the bulk modulus κ will tend to infinity based on Eq. (5). Then, the bilinear
165 form c in Eq. (11) tends to zero. And the weak form of Eq. (14) becomes an
166 enforcement of the volumetric strain $\nabla \cdot \mathbf{u}_h$ to be zero using the Lagrangian
167 multiplier method, where p_h is the Lagrangian multiplier.

168 Furthermore, from the second line of Eq. (14), we have:

$$b(\mathbf{u}_h, q_h) + c(q_h, p_h) = (q_h, \nabla \cdot \mathbf{u}_h) - (q_h, \frac{1}{3\kappa} p_h) = 0, \quad \forall q_h \in Q_h \quad (15)$$

169 or

$$(q_h, 3\kappa \nabla \cdot \mathbf{u}_h - p_h) = 0, \quad \forall q_h \in Q_h \quad (16)$$

170 where (\bullet, \bullet) is the inner product operator evaluated by:

$$(q, p) := \int_{\Omega} q p d\Omega \quad (17)$$

171 Obviously, in Eq. (16), p_h is the orthogonal projection of $3\kappa \nabla \cdot \mathbf{u}_h$ with respect
172 to the space Q_h [1], and, for further development, we use the nabla notation

¹⁷³ with an upper tilde to denote the projection operator, i.e., $p_h = \tilde{\nabla} \cdot \mathbf{u}_h$. In this
¹⁷⁴ circumstance, the bilinear form b in the first line of Eq. (14) becomes:

$$\begin{aligned} b(\mathbf{v}_h, p_h) &= \underbrace{(\nabla \cdot \mathbf{v}_h - \tilde{\nabla} \cdot \mathbf{v}_h, p_h)}_0 + (\tilde{\nabla} \cdot \mathbf{v}_h, \underbrace{p_h}_{3\kappa \tilde{\nabla} \cdot \mathbf{u}_h}) \\ &= (\tilde{\nabla} \cdot \mathbf{v}_h, 3\kappa \tilde{\nabla} \cdot \mathbf{u}_h) \\ &= \tilde{a}(\mathbf{v}_h, \mathbf{u}_h) \end{aligned} \quad (18)$$

¹⁷⁵ where the bilinear form $\tilde{a} : V_h \times V_h \rightarrow \mathbb{R}$ is defined by:

$$\tilde{a}(\mathbf{v}_h, \mathbf{u}_h) = \int_{\Omega} 3\kappa \tilde{\nabla} \cdot \mathbf{v}_h \tilde{\nabla} \cdot \mathbf{u}_h d\Omega \quad (19)$$

¹⁷⁶ Accordingly, the problem of Eq. (14) becomes a one-variable form: Find
¹⁷⁷ $\mathbf{u}_h \in V_h$, such that

$$a(\mathbf{v}_h, \mathbf{u}_h) + \tilde{a}(\mathbf{v}_h, \mathbf{u}_h) = f(\mathbf{v}_h), \quad \forall \mathbf{v}_h \in V_h \quad (20)$$

¹⁷⁸ As $\kappa \rightarrow \infty$, Eq. (20) can be regarded as an enforcement of volumetric strain
¹⁷⁹ using the penalty method, where \tilde{a} is the penalty term. However, it should
¹⁸⁰ be noted that, if the mixed-formulation wants to obtain a satisfactory result,
¹⁸¹ this orthogonal projection must be surjective [57]. In the case where it is not
¹⁸² surjective, for a given $p_h \in Q_h$, it may not be possible to find a $\mathbf{u}_h \in V_h$ such that
¹⁸³ $p_h = 3\kappa \tilde{\nabla} \cdot \mathbf{u}_h$. This will lead to a much smaller displacement than expected and
¹⁸⁴ an oscillated pressure result. This phenomenon is called volumetric locking.

¹⁸⁵ 3. Optimal volumetric constraint ratio

¹⁸⁶ 3.1. Inf-sup condition and its eigenvalue problem

¹⁸⁷ To ensure the surjectivity of orthogonal projection and satisfactory results,
¹⁸⁸ the approximations of Eq.(7) should satisfy the inf-sup condition, also known
¹⁸⁹ as the LadyzhenskayaBabuкаBrezzi condition [4]:

$$\inf_{q_h \in Q_h} \sup_{\mathbf{v}_h \in V_h} \frac{|b(q_h, \mathbf{v}_h)|}{\|q_h\|_Q \|\mathbf{v}_h\|_V} \geq \beta > 0 \quad (21)$$

¹⁹⁰ in which β , namely the inf-sup value, is a constant independent of the charac-
¹⁹¹ terized element size h . The norms $\|\bullet\|_V$ and $\|\bullet\|_Q$ can be flexibly defined
¹⁹² by:

$$\|\mathbf{v}\|_V^2 := \int_{\Omega} \nabla^d \mathbf{v} : \nabla^d \mathbf{v} d\Omega \quad (22)$$

$$\|q\|_Q^2 := \int_{\Omega} \frac{1}{3\kappa} q^2 d\Omega \quad (23)$$

¹⁹³ To establish the relationship between the inf-sup condition and the con-
¹⁹⁴ straint ratio, the inf-sup condition is firstly transformed by the following Lemma
¹⁹⁵ 1:

196 **Lemma 1.** Suppose $\mathcal{P}_h : V_h \rightarrow Q_h$ is the orthogonal projection operator of the
197 divergence operator $\mathcal{P} := 3\kappa \nabla \cdot$, i.e., $\mathcal{P}_h := 3\kappa \bar{\nabla} \cdot$ and satisfies Eq. (16). Then,
198 the inf-sup value can be estimated by:

$$\beta \leq \inf_{V'_h \subset V_h \setminus \ker \mathcal{P}_h} \sup_{\mathbf{v}_h \in V'_h} \frac{\|\mathcal{P}_h \mathbf{v}_h\|_Q}{\|\mathbf{v}_h\|_V} \quad (24)$$

199 in which $\ker \mathcal{P}_h \subset V_h$ is the kernel of \mathcal{P}_h defined by $\ker \mathcal{P}_h := \{\mathbf{v}_h \in V_h \mid \mathcal{P}_h \mathbf{v}_h =$
200 0\}.

201 PROOF. First, define the image space of \mathcal{P}_h as $\text{Im}\mathcal{P}_h := \{p_h \in Q_h \mid \exists \mathbf{v}_h \in$
202 $V_h, p_h = \mathcal{P}_h \mathbf{v}_h\}$. Since $\mathcal{P}_h \subset Q_h$, Eq. (21) can be rewritten as:

$$\begin{aligned} \beta &\leq \inf_{q_h \in Q_h} \sup_{\mathbf{v}_h \in V_h} \frac{|b(q_h, \mathbf{v}_h)|}{\|q_h\|_Q \|\mathbf{v}_h\|_V} = \inf_{q_h \in Q_h} \sup_{\mathbf{v}_h \in V_h} \frac{|(q_h, \frac{1}{3\kappa} \mathcal{P} \mathbf{v}_h)|}{\|q_h\|_Q \|\mathbf{v}_h\|_V} \\ &\leq \inf_{q_h \in \text{Im}\mathcal{P}_h} \sup_{\mathbf{v}_h \in V_h} \frac{|\frac{1}{3\kappa} (q_h, \mathcal{P}_h \mathbf{v}_h)|}{\|q_h\|_Q \|\mathbf{v}_h\|_V} \end{aligned} \quad (25)$$

203 For a given $q_h \in \text{Im}\mathcal{P}_h$, suppose a space $V'_h \subseteq V_h \setminus \ker \mathcal{P}_h$ defined by:

$$V'_h = \{\mathbf{v}_h \in V_h \mid \mathcal{P}_h \mathbf{v}_h = q_h\} \quad (26)$$

204 Since $\text{Im}\mathcal{P}_h \subset Q_h$, according to the Cauchy-Schwarz inequality, we have:

$$\left| \frac{1}{3\kappa} (q_h, \mathcal{P}_h \mathbf{v}_h) \right| \leq \|q_h\|_Q \|\mathcal{P}_h \mathbf{v}_h\|_Q \quad (27)$$

205 where this equality holds if and only if $q_h = \mathcal{P}_h \mathbf{v}_h$, i.e.,

$$\left| \frac{1}{3\kappa} (q_h, \mathcal{P}_h \mathbf{v}_h) \right| = \|q_h\|_Q \|\mathcal{P}_h \mathbf{v}_h\|_Q, \quad \forall \mathbf{v}_h \in V'_h \quad (28)$$

206 And the following relationship can be evidenced:

$$\sup_{\mathbf{v}_h \in V_h} \frac{|\frac{1}{3\kappa} (q_h, \mathcal{P}_h \mathbf{v}_h)|}{\|q_h\|_Q \|\mathbf{v}_h\|_V} = \sup_{\mathbf{v}_h \in V'_h} \frac{\|\mathcal{P}_h \mathbf{v}_h\|_Q}{\|\mathbf{v}_h\|_V}, \quad \forall q_h \in \text{Im}\mathcal{P}_h \quad (29)$$

207 Consequently, by combining Eqs. (25) and (29), Eq. (24) can be obtained.

208 **Remark 1.** With Lemma 1 and the norm definitions in Eqs. (22),(23), the
209 square of the inf-sup value can further be bounded by:

$$\beta^2 \leq \inf_{V'_h \subset V_h \setminus \ker \mathcal{P}_h} \sup_{\mathbf{v}_h \in V'_h} \frac{\|\mathcal{P}_h \mathbf{v}_h\|_Q^2}{\|\mathbf{v}_h\|_V^2} = \inf_{V'_h \subset V_h \setminus \ker \mathcal{P}_h} \sup_{\mathbf{v}_h \in V'_h} \frac{\tilde{a}(\mathbf{v}_h, \mathbf{v}_h)}{a(\mathbf{v}_h, \mathbf{v}_h)} \quad (30)$$

210 The left-hand side of the above equation is consistent with the minimum-maximum
211 principle [58] and again proves the equivalence with the traditional numerical
212 inf-sup test [5]. Since that, β^2 evaluates the non-zero general eigenvalue of \tilde{a}
213 and a in Eq. (20).

214 3.2. Inf-sup value estimator

215 Subsequently, the relationship between constraint ratio and the inf-sup condition is established by the following Theorem:

217 **Theorem 1.** Suppose that P_{n_u} is a complete polynomial space with n_u dimensions, and V_{n_u} is the polynomial displacement space, $V_{n_u} = P_{n_u}^{n_d}$. The inf-sup value β can further be bounded by:

$$\beta \leq \beta_s + O(h) \quad (31)$$

220 with

$$\beta_s = \inf_{V' \subset V_{n_u} \setminus \ker \mathcal{P}_h \mathcal{I}_h} \sup_{\mathbf{v} \in V'} \frac{\|\mathcal{P}\mathbf{v}\|_Q}{\|\mathbf{v}\|_V} \quad (32)$$

221 where \mathcal{I}_h is the interpolation operator of the finite element approximation, and
222 correspondingly, $O(h)$ is the remainder related to h .

223 PROOF. As the dimensions of V_h and V_{n_u} are identical, $\dim V_{n_u} = \dim V_h =$
224 $n_d \times n_u$. There exists a unique $\mathbf{v} \in V_{n_u}$ satisfying $\mathbf{v}_h = \mathcal{I}_h \mathbf{v}$. And the right side
225 of Eq. (24) becomes:

$$\inf_{V'_h \subset V_h \setminus \ker \mathcal{P}_h} \sup_{\mathbf{v}_h \in V'_h} \frac{\|\mathcal{P}_h \mathbf{v}_h\|_Q}{\|\mathbf{v}_h\|_V} = \inf_{V' \subset V_{n_u} \setminus \ker \mathcal{P}_h \mathcal{I}_h} \sup_{\mathbf{v} \in V'} \frac{\|\mathcal{P}_h \mathcal{I}_h \mathbf{v}\|_Q}{\|\mathcal{I}_h \mathbf{v}\|_V} \quad (33)$$

226 According to the triangular inequality, Cauchy-Schwarz inequality, and the
227 relationship of Eqs. (16), we have:

$$\begin{aligned} \|\mathcal{P}_h \mathcal{I}_h \mathbf{v}\|_Q &= \sup_{q_h \in Q_h} \frac{|\frac{1}{3\kappa}(q_h, \mathcal{P}_h \mathcal{I}_h \mathbf{v})|}{\|q_h\|_Q} = \sup_{q_h \in Q_h} \frac{|\frac{1}{3\kappa}(q_h, \mathcal{P} \mathcal{I}_h \mathbf{v})|}{\|q_h\|_Q} \\ &\leq \sup_{q_h \in Q_h} \frac{|\frac{1}{3\kappa}(q_h, \mathcal{P} \mathbf{v})| + |\frac{1}{3\kappa}(q_h, \mathcal{P} \mathbf{v} - \mathcal{P} \mathcal{I}_h \mathbf{v})|}{\|q_h\|_Q} \quad (34) \\ &\leq \|\mathcal{P} \mathbf{v}\|_Q + \|\mathcal{P}(\mathbf{v} - \mathcal{I}_h \mathbf{v})\|_Q \end{aligned}$$

228 Obviously, the second term on the right side of Eq. (34) is the interpolation
229 error, and can be evaluated by [59]:

$$\|\mathcal{P}(\mathbf{v} - \mathcal{I}_h \mathbf{v})\|_Q \leq Ch^k |\mathbf{v}|_{H_k} \quad (35)$$

230 where, for a sufficiently smooth $\mathbf{v} \in V$, k equals to the interpolation order of
231 \mathcal{I}_h .

232 Further leading the relation $\|\mathcal{I}_h \mathbf{v}\|_V \geq C |\mathbf{v}|_{H_k}$ obtained from the closed
233 graph theorem [33] and considering Eqs. (34)-(35), the right-hand side of Eq.
234 (33) can be represented as:

$$\inf_{V' \subset V_{n_u} \setminus \ker \mathcal{P}_h \mathcal{I}_h} \sup_{\mathbf{v} \in V'} \frac{\|\mathcal{P}_h \mathcal{I}_h \mathbf{v}\|_Q}{\|\mathcal{I}_h \mathbf{v}\|_V} \leq \inf_{V' \subset V_{n_u} \setminus \ker \mathcal{P}_h \mathcal{I}_h} \sup_{\mathbf{v} \in V'} \frac{\|\mathcal{P} \mathbf{v}\|_Q}{\|\mathbf{v}\|_V} + O(h) \quad (36)$$

235 Substituting Eqs. (33),(36) into (24) finally proves Eqs. (31), (32).

236 As we can see in Eqs. (31) and (32), $\beta_s \geq 0$, the condition β_s being equal to
 237 0 or not determines whether the formulation can satisfy the inf-sup condition.
 238 If $\beta_s > 0$, as the mesh refines, the second term on the right-hand side of Eq.
 239 (31) will sharply reduce and can be ignored. In contrast, if $\beta_s = 0$, the second
 240 term will dominate, and the evaluation of β will be dependent to h . Therefore,
 241 the inf-sup condition is violated and numerical instability arises.

242 3.3. Polynomial-wise constraint counting

243 From the above subsection, we can know that whether β_s is zero or not
 244 determines whether the mixed-formulation can fulfill the inf-sup condition. Ac-
 245 cording to the expression of β_s in Eq. (32), as $\beta_s = 0$, the variable \mathbf{v} should
 246 belong to $\ker \mathcal{P}$, so the dimensions of the subspace in which $\beta_s \neq 0$, namely n_s ,
 247 can be evaluated by:

$$n_s = \dim(V_{n_u} \setminus \ker \mathcal{P}) \quad (37)$$

248 To further construct the relationship between the inf-sup value estimator in
 249 Eq. (31) and the constraint ratio $r = \frac{n_d \times n_u}{n_p}$, we should find the displacement
 250 and pressure DOFs in Eq. (31). With the definition of V_{n_u} , the number of
 251 displacement DOFs is easy to be evaluated by:

$$n_d \times n_u = \dim V_{n_u} \quad (38)$$

252 With well-posed nodal distributions of displacement and pressure, the number
 253 of pressure DOFs has the following relationship:

$$n_p = \dim Q_h = \dim(\text{Im} \mathcal{P}_h) = \dim(V_{n_u} \setminus \ker \mathcal{P}_h \mathcal{I}_h) \quad (39)$$

254 Figure 1 illustrates how the relationship between n_s , n_p , and n_u influences
 255 the fulfillment of the inf-sup condition:

- 256 As $n_p > n_s$, there must exist a subspace in space $V_{n_u} \setminus \ker \mathcal{P}_h \mathcal{I}_h$ belonging
 257 to $\ker \mathcal{P}$, resulting in $\beta_s = 0$, i.e., $V_{n_u} \setminus \ker \mathcal{P}_h \mathcal{I}_h \cap \ker \mathcal{P} \neq \emptyset$. At this cir-
 258 cumstance, the inf-sup condition cannot be satisfied, and the formulation
 259 will suffer from volumetric locking.
- 260 As $n_p \leq n_s$, for well-posed nodal distributions, the space $V_{n_u} \setminus \ker \mathcal{P}_h \mathcal{I}_h$
 261 may be a subset of $V_{n_u} \setminus \ker \mathcal{P}$. Then, β_s will remain nonzero, and the
 262 formulation will be locking-free.

263 Summarily, the formulation can satisfy the inf-sup condition and alleviate
 264 volumetric locking if at least the number of pressure nodes n_p is less than n_s ,
 265 so we name n_s as the stabilized number of pressure nodes. At this moment,
 266 the volumetric constraint ratio should meet the following relation to ensure the
 267 inf-sup condition:

$$r_{opt} \geq \frac{n_d \times n_u}{n_s} \quad (40)$$

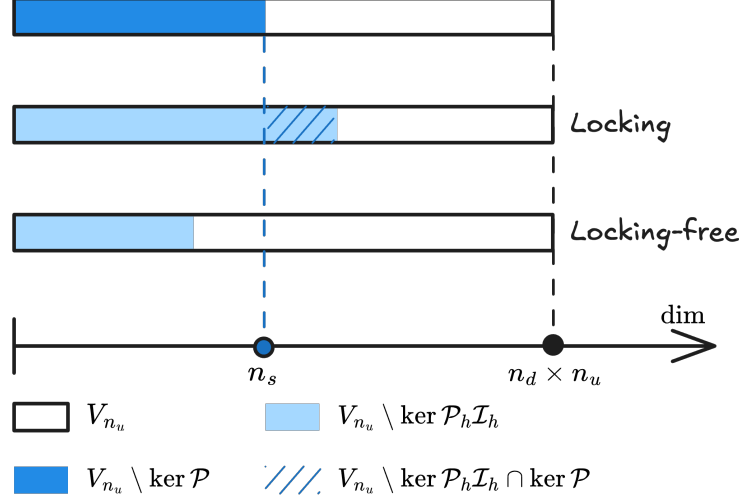


Figure 1: Illustration of estimator

268 **Remark 2.** Some uniform elements with special arrangements, like the union-
 269 jack element arrangement for 3-node triangular elements, can pass the inf-sup
 270 test [6], but their pressure DOFs number is greater than n_s . This is because the
 271 union-jack arrangement leads to a lower nonzero eigenvalue number of \tilde{a} and a
 272 in Eq. (20), and the corresponding nonzero eigenvalue number is less than or
 273 equal to the stabilized number n_s , satisfying Eq. (40). The similar cases about
 274 this special element arrangement are too few, so it is more straightforward to
 275 use the number of pressure nodes n_p to measure $\dim(V_{n_u} \setminus \ker \mathcal{P}_h \mathcal{I}_h)$.

276 **Remark 3.** It is obvious that the traditional optimal constraint ratio cannot
 277 fulfill this condition. However, not all formulations satisfying this condition can
 278 totally avoid volumetric locking. This is because $n_p \leq n_s$ is not equivalent to
 279 $V_{n_u} \setminus \ker \mathcal{P}_h \mathcal{I}_h \subset V_{n_u} \setminus \ker \mathcal{P}$. Fortunately, well-posed nodal distributions of
 280 displacement and pressure can ensure this, which will be evidenced by numerical
 281 examples in the subsequent sections.

282 3.4. Optimal volumetric constraint ratio

283 The fulfillment of the inf-sup condition should require the number of pres-
 284 sure nodes n_p to be lower than the stabilized number n_s , and now, we will
 285 demonstrate how to determine n_s for a specific number of displacement DOFs.

286 In the 2D case, for instance, we first consider the linear polynomial displace-
 287 ment space V_3 that is given by:

$$288 V_3 = \text{span} \left\{ \begin{pmatrix} 1 \\ 0 \end{pmatrix}, \begin{pmatrix} 0 \\ 1 \end{pmatrix}, \begin{pmatrix} x \\ 0 \end{pmatrix}, \begin{pmatrix} 0 \\ x \end{pmatrix}, \begin{pmatrix} y \\ 0 \end{pmatrix}, \begin{pmatrix} 0 \\ y \end{pmatrix} \right\} \quad (41)$$

²⁸⁸ or rearranged as follows,

$$V_3 = \text{span} \left\{ \underbrace{\left(\begin{matrix} 1 \\ 0 \end{matrix} \right), \left(\begin{matrix} 0 \\ 1 \end{matrix} \right), \left(\begin{matrix} y \\ 0 \end{matrix} \right), \left(\begin{matrix} 0 \\ x \end{matrix} \right), \left(\begin{matrix} x \\ -y \end{matrix} \right)}_{\ker \mathcal{P}}, \underbrace{\left(\begin{matrix} x \\ y \end{matrix} \right)}_{V_3 \setminus \ker \mathcal{P}} \right\} \quad (42)$$

²⁸⁹ It can be counted that, for $n_u = 3$, $n_s = 1$. Following the path, the displacement
²⁹⁰ space with a quadratic polynomial base, namely V_6 , can be stated as:

$$V_6 = \text{span} \left\{ \underbrace{\left(\begin{matrix} 1 \\ 0 \end{matrix} \right), \left(\begin{matrix} 0 \\ 1 \end{matrix} \right), \left(\begin{matrix} y \\ 0 \end{matrix} \right), \left(\begin{matrix} 0 \\ x \end{matrix} \right), \left(\begin{matrix} x \\ -y \end{matrix} \right), \left(\begin{matrix} x^2 \\ -2xy \end{matrix} \right), \left(\begin{matrix} y^2 \\ 0 \end{matrix} \right), \left(\begin{matrix} 0 \\ x^2 \end{matrix} \right), \left(\begin{matrix} -2xy \\ y^2 \end{matrix} \right)}_{\ker \mathcal{P}}, \underbrace{\left(\begin{matrix} x \\ y \end{matrix} \right), \left(\begin{matrix} x^2 \\ 2xy \end{matrix} \right), \left(\begin{matrix} 2xy \\ y^2 \end{matrix} \right)}_{V_6 \setminus \ker \mathcal{P}} \right\} \quad (43)$$

²⁹¹ In this circumstance, $n_s = 3$. As the order of the polynomial space increases,
²⁹² the optimal numbers of constraint DOFs for each order of the polynomial space
²⁹³ are listed in Table. 1, in which n denotes the order of space P_{n_u} . For the
²⁹⁴ flexibility of usage, the relation between n_u and n_s is summarized as follows:

$$n_s = \frac{n(n+1)}{2}, \quad n = \left\lfloor \frac{\sqrt{1+8n_u}-3}{2} \right\rfloor \quad (44)$$

²⁹⁵ where $\lfloor \bullet \rfloor$ denotes the floor function.

Table 1: Relationship between the number of displacement nodes n_u and stabilized number of pressure nodes n_s

n	2D		3D	
	n_u	n_s	n_u	n_s
1	3	1	4	1
2	6	3	10	4
3	10	6	20	10
4	15	10	35	20
\vdots	\vdots	\vdots	\vdots	\vdots

²⁹⁶ For the 3D case, following the path in 2D, the linear polynomial space V_4 is

²⁹⁷ considered herein, and the arranged space of V_4 is listed as follows:

$$V_4 = \text{span} \left\{ \underbrace{\begin{pmatrix} 1 \\ 0 \\ 0 \\ 0 \end{pmatrix}, \begin{pmatrix} 0 \\ 1 \\ 0 \\ 0 \end{pmatrix}, \begin{pmatrix} 0 \\ 0 \\ 1 \\ 0 \end{pmatrix}, \begin{pmatrix} 0 \\ x \\ 0 \\ 0 \end{pmatrix}, \begin{pmatrix} 0 \\ 0 \\ x \\ 0 \end{pmatrix}, \begin{pmatrix} y \\ 0 \\ 0 \\ 0 \end{pmatrix}}_{\ker \mathcal{P}}, \underbrace{\begin{pmatrix} 0 \\ 0 \\ z \\ 0 \end{pmatrix}, \begin{pmatrix} 0 \\ 0 \\ z \\ 0 \end{pmatrix}, \begin{pmatrix} 0 \\ 0 \\ 0 \\ 1 \end{pmatrix}, \begin{pmatrix} x \\ -y \\ 0 \\ 0 \end{pmatrix}, \begin{pmatrix} x \\ 0 \\ -z \\ 0 \end{pmatrix}, \begin{pmatrix} x \\ y \\ z \\ 0 \end{pmatrix}}_{V_{n_u} \setminus \ker \mathcal{P}} \right\} \quad (45)$$

²⁹⁸ For brevity, the stabilized numbers for higher-order polynomial displacement
²⁹⁹ spaces are directly listed in Table. 1, and it can be summarized that, for a given
³⁰⁰ number of displacement DOFs, the stabilized number for pressure DOFs can be
³⁰¹ calculated as follows:

$$n_s = \frac{n(n+1)(n+2)}{6} \quad (46)$$

$$n = \left[\left(3n_u + \frac{1}{3} \sqrt{81n_u^2 - \frac{1}{3}} \right)^{\frac{1}{3}} + \frac{1}{3 \left(3n_u + \frac{1}{3} \sqrt{81n_u^2 - \frac{1}{3}} \right)^{\frac{1}{3}}} - 2 \right] \quad (47)$$

³⁰² 4. Mixed FE–meshfree formulation with optimal constraint ratio

³⁰³ In the proposed mixed–formulation, the displacement is approximated using
³⁰⁴ 3-node (Tri3), 6-node (Tri6) triangular elements and 4-node (Quad4), 8-node
³⁰⁵ (Quad8) quadrilateral elements in 2D, 4-node (Tet4) tetrahedral element and
³⁰⁶ 8-node(Hex8) hexahedral element in 3D [2]. In order to flexibly adjust to let the
³⁰⁷ DOFs of pressure meet the optimal constraint, the reproducing kernel meshfree
³⁰⁸ approximation is involved to approximate pressure.

³⁰⁹ 4.1. Reproducing kernel meshfree approximation

³¹⁰ In accordance with the reproducing kernel approximation, the entire domain
³¹¹ Ω , as shown in Figure 2, is discretized by n_p meshfree nodes, $\{\mathbf{x}_I\}_{I=1}^{n_p}$. The
³¹² approximated pressure, namely p_h , can be expressed by the shape function Ψ_I
³¹³ and nodal coefficient p_I , yields:

$$p_h(\mathbf{x}) = \sum_{I=1}^{n_p} \Psi_I(\mathbf{x}) p_I \quad (48)$$

³¹⁴ where, in the reproducing kernel approximation framework, the shape function
³¹⁵ Ψ_I is given by:

$$\Psi_I(\mathbf{x}) = \mathbf{c}(\mathbf{x}_I - \mathbf{x}) \mathbf{p}(\mathbf{x}_I - \mathbf{x}) \phi(\mathbf{x}_I - \mathbf{x}) \quad (49)$$

³¹⁶ in which \mathbf{p} is the basis vector, for instance in the context of the 3D quadratic
³¹⁷ case, the basis vector takes the following form:

$$\mathbf{p}(\mathbf{x}) = \{1, x, y, z, x^2, y^2, z^2, xy, xz, yz\}^T \quad (50)$$

³¹⁸ and ϕ stands for the kernel function. In this work, the traditional Cubic B-spline
³¹⁹ function with square or cube support is used as the kernel function:

$$\phi(\mathbf{x}_I - \mathbf{x}) = \phi(s_x)\phi(s_y)\phi(s_z), \quad s_i = \frac{\|\mathbf{x}_I - \mathbf{x}\|}{\bar{s}_{iI}} \quad (51)$$

³²⁰ with

$$\phi(s) = \frac{1}{3!} \begin{cases} (2-2s)^3 - 4(1-2s)^3 & s \leq \frac{1}{2} \\ (2-2s)^3 & \frac{1}{2} < s < 1 \\ 0 & s > 1 \end{cases} \quad (52)$$

³²¹ where \bar{s}_{iI} 's are the support size towards the i -direction for the shape function
³²² Ψ_I . The correction function \mathbf{c} can be determined by the following so-called
³²³ consistency condition:

$$\sum_{I=1}^{n_p} \Psi_I(\mathbf{x}) \mathbf{p}(\mathbf{x}_I) = \mathbf{p}(\mathbf{x}) \quad (53)$$

³²⁴ or equivalent shifted form:

$$\sum_{I=1}^{n_p} \Psi_I(\mathbf{x}) \mathbf{p}(\mathbf{x}_I - \mathbf{x}) = \mathbf{p}(\mathbf{0}) \quad (54)$$

³²⁵ The consistency condition ensures that the reproducing kernel shape functions
³²⁶ is able to reproduce the polynomial spanned by base function \mathbf{p} , which is the
³²⁷ requirement for the accuracy of Galerkin method. And herein, the order of base
³²⁸ function \mathbf{p} is chosen to be the same as the order of displacement approximation.

³²⁹ Further, substituting Eq. 49 into Eq. (54) leads to:

$$\mathbf{c}(\mathbf{x}_I - \mathbf{x}) = \mathbf{A}^{-1}(\mathbf{x}_I - \mathbf{x}) \mathbf{p}(\mathbf{0}) \quad (55)$$

³³⁰ in which \mathbf{A} is namely the moment matrix evaluated by:

$$\mathbf{A}(\mathbf{x}_I - \mathbf{x}) = \sum_{I=1}^{n_p} \mathbf{p}(\mathbf{x}_I - \mathbf{x}) \mathbf{p}^T(\mathbf{x}_I - \mathbf{x}) \phi(\mathbf{x}_I - \mathbf{x}) \quad (56)$$

³³¹ Taking Eq. (55) back to Eq. (49), the final form of the reproducing kernel shape
³³² function can be obtained as:

$$\Psi_I(\mathbf{x}) = \mathbf{p}^T(\mathbf{0}) \mathbf{A}^{-1}(\mathbf{x}_I - \mathbf{x}) \phi(\mathbf{x}_I - \mathbf{x}) \quad (57)$$

³³³ As shown in Figure 2, reproducing kernel meshfree shape functions are glob-
³³⁴ ally smooth across the entire domain, using them to discretize the pressure field
³³⁵ allows the constraint ratio to be adjusted arbitrarily, without being limited by

element topology. Moreover, when combined with finite element approximations in Eq. 14, numerical integration can be conveniently performed within each finite element (Ω_C 's). The numerical integration issue caused by the loss of variational consistency between meshfree shape functions and their derivatives would not appear in mixed formulation of Eq. 14, since Eq. 14 only needs meshfree shape functions itself. Consequently, the proposed methods just need to employ the standard lower order Gaussian quadrature rules used in traditional finite element methods to ensure the accuracy.

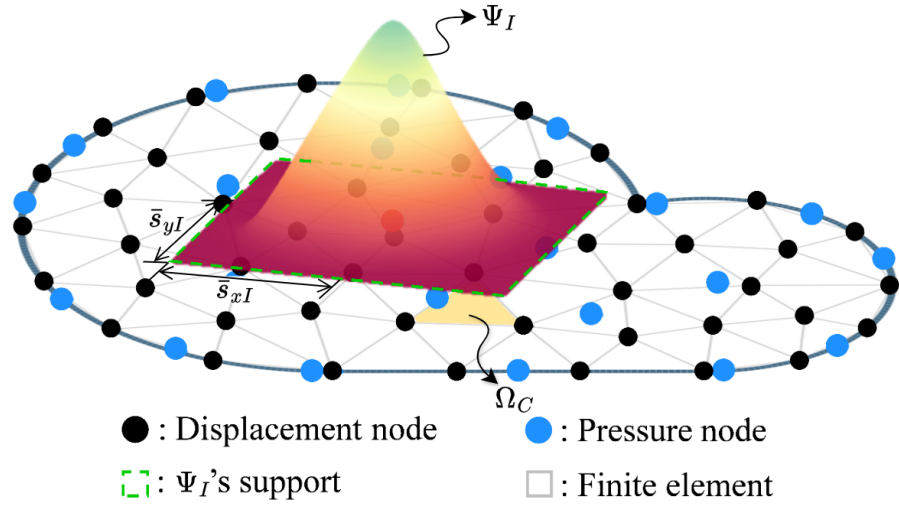


Figure 2: Illustration for reproducing kernel meshfree approximation

4.2. Pressure node distributions with optimal constraint ratio

In this subsection, 2D and 3D inf-sup tests [6], as defined in Eq. 30, are conducted using the mixed FEmeshfree formulations to validate the proposed inf-sup value estimator. The 2D test considers the square domain $\Omega = (0, 1) \times (0, 1)$, where the displacement is discretized by Tri3 element, Quad4 element with 4×4 , 8×8 , 16×16 and 32×32 elements, Tri6 element, Quad8 element with 2×2 , 4×4 , 8×8 and 16×16 elements, respectively. The 3D test employs a cube domain $\Omega = (0, 1) \times (0, 1) \times (0, 1)$ with 4×4 , 8×8 and 16×16 elements for the Tet4 element and Hex8 element. The pressure discretization is performed that, linear meshfree approximation with normalized support size 1.5 is used for Tri3, Quad4, Tet4 elements, and the quadratic meshfree approximation with normalized support size 2.5 is used for Tri6, Quad8, Hex8 elements. In order to avoid the influence of interpolation error, uniform nodal distributions are used for pressure discretizations, for example the 4×4 Quad4 elements with 4×3 uniform pressure nodes.

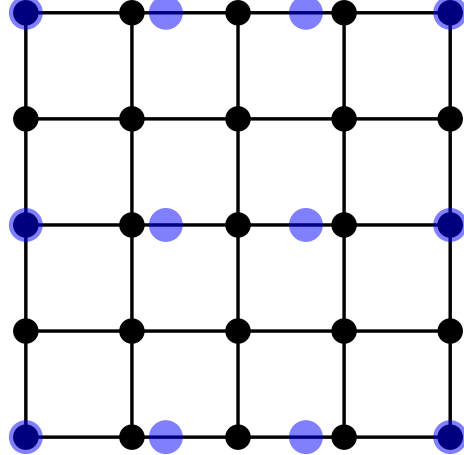


Figure 3: Illustration of uniform nodal distribution for inf-sup test with $n_u = 5 \times 5$, $n_p = 4 \times 3$

Figures 4–9 show the corresponding results, in which the red line stands for the value of β with respect to the number of pressure nodes n_p , and the vertical dashed line denotes the stabilized number n_s . The deeper color of the lines means mesh refinement. The results show that, no matter linear or quadratic elements, as n_p increases over n_s , the value of β sharply decreases, and then the inf-sup condition cannot be maintained. This result is consistent with the discussion in Section 3, and again verifies the effect of the proposed estimator.

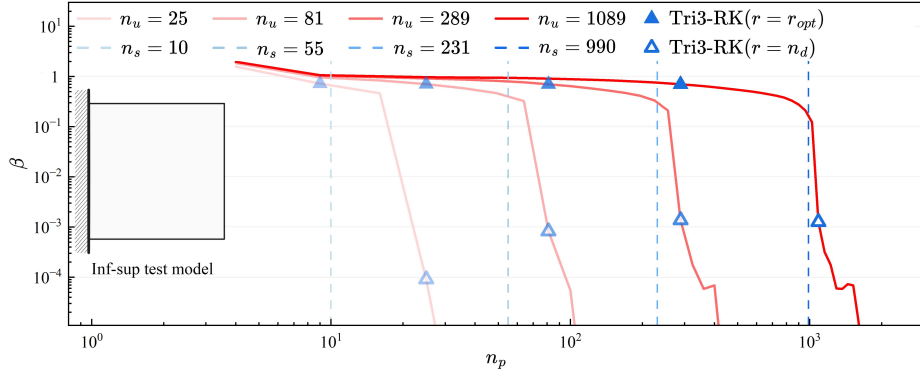


Figure 4: Inf-sup test for Tri3-RK

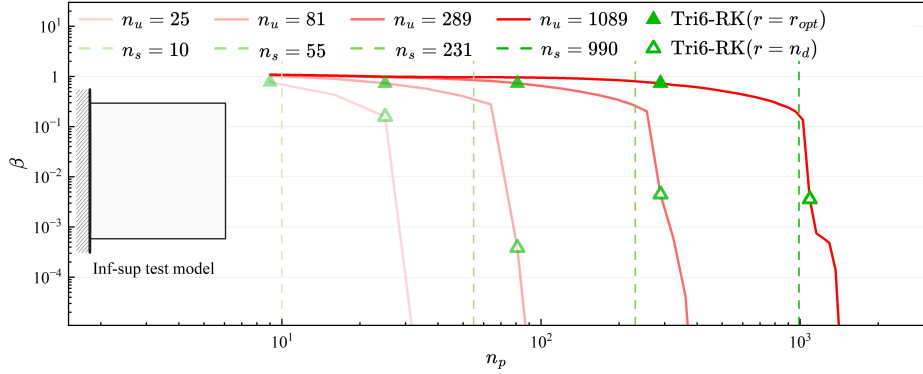


Figure 5: Inf-sup test for Tri6-RK

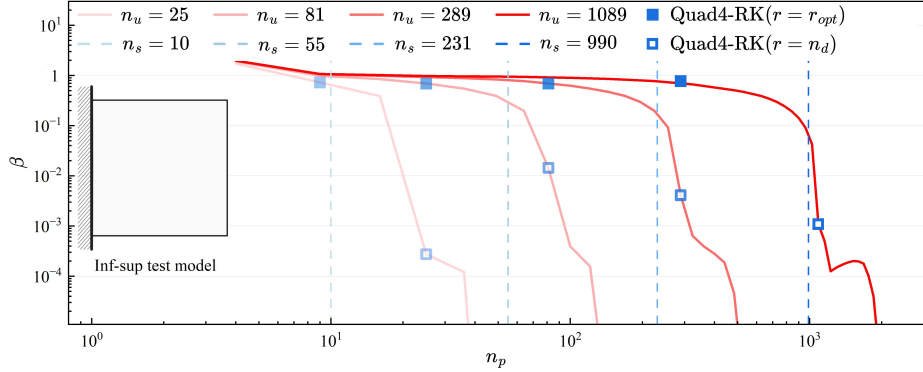


Figure 6: Inf-sup test for Quad4-RK

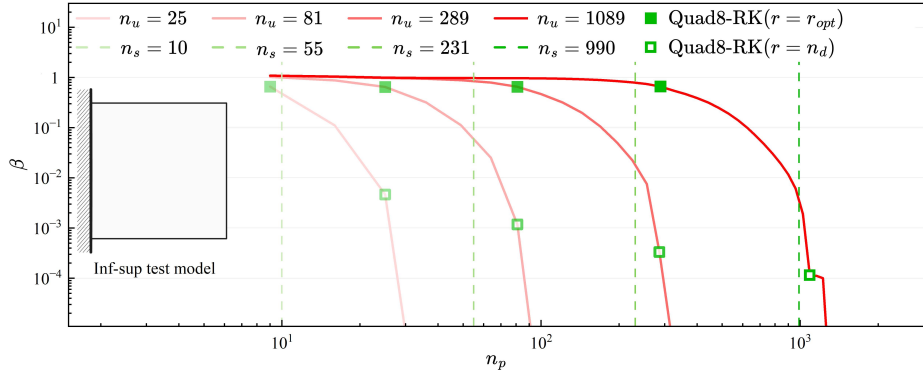


Figure 7: Inf-sup test for Quad8-RK

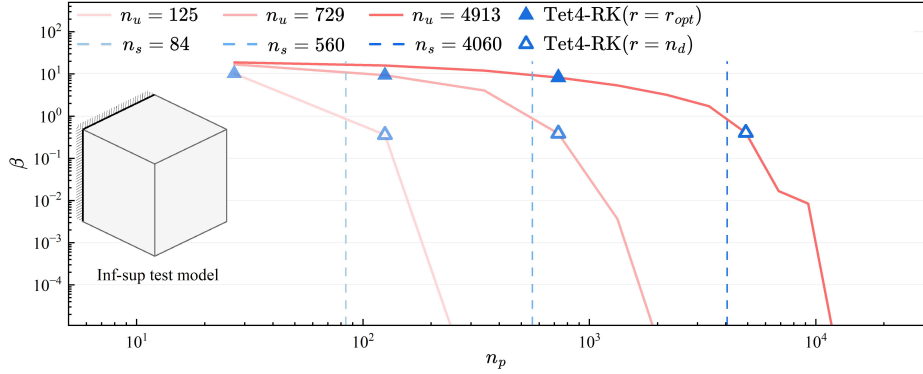


Figure 8: Inf-sup test for Tet4-RK

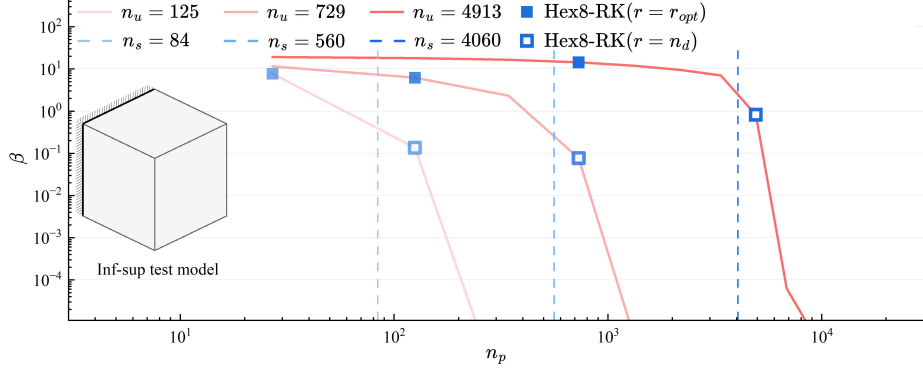


Figure 9: Inf-sup test for Hex8-RK

366 Moreover, the mixed formulation's results with the traditional optimal con-
 367 straint ratio $r = n_d$ are listed in these figures as well, and β in this circumstance
 368 is already much smaller than those in the optimal range. Considering the re-
 369 sults shown above, the easy programming and efficiency, the pressure nodes
 370 are chosen among the displacement nodes. The optimal schemes for linear and
 371 quadratic, 2D and 3D element discretizations, namely with $r = r_{opt}$, are shown
 372 in Figure 10, where every other displacement node is selected as the pressure
 373 node. For practical implementation of linear cases, the pressure nodes are firstly
 374 generated by traditional approaches, like the Delaunay triangulation, and then
 375 the displacement nodes can be obtained by a standard mesh refinement process.
 376 For the quadratic approximation of Tri6 and Quad8 elements, the vertices of
 377 the elements are selected as pressure nodes after displacement element genera-
 378 tion. As a result all constraint ratios evaluated using discretizations in Figure
 379 10 belong to the range of the optimal ratio. The corresponding inf-sup test
 380 results for these schemes are also marked in inf-sup test figure and show that,
 381 with mesh refinement, their β 's are always maintained at a non-negligible level.

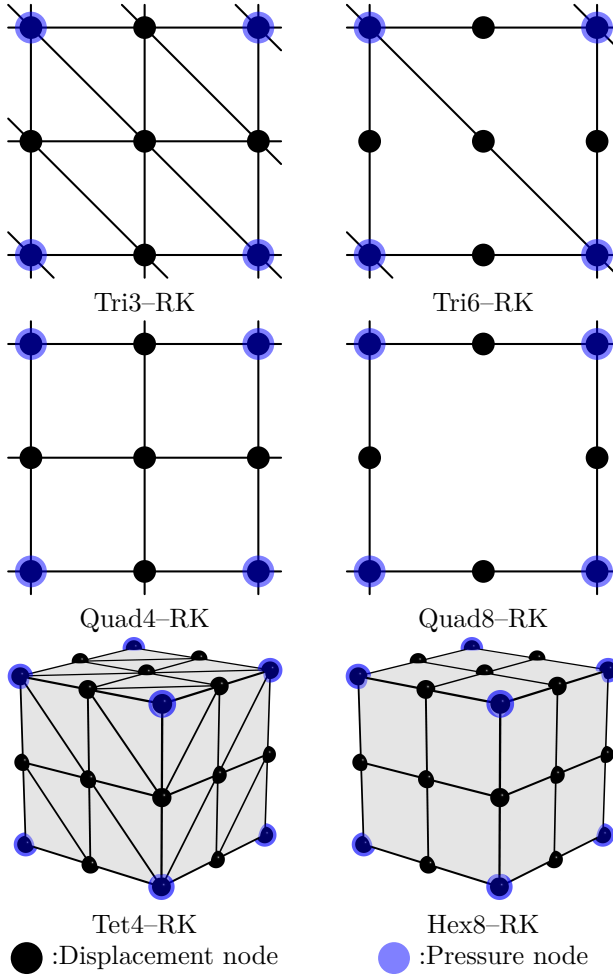


Figure 10: Nodal distribution schemes for mixed FE-meshfree formulations with $r = r_{opt}$

382 **5. Numerical examples**

383 **5.1. Cantilever beam problem**

384 Consider the cantilever beam problem shown in Figure 11 with length $L =$
 385 48 , width $D = 12$, and the incompressible material parameters are employed
 386 with Young's modulus $E = 3 \times 10^6$, Poisson's ratio $\nu = 0.5 - 10^{-8}$. The left hand
 387 side is fixed and the right side subject to a concentrated force $P = 1000$. All
 388 the prescribed values in the boundary conditions are evaluated by the analytical

³⁸⁹ solution that is given as follows [60]:

$$\begin{cases} u_x(x) = -\frac{Py}{6\bar{E}I} \left((6L - 3x)x + (2 + \bar{\nu})(y^2 - \frac{D^2}{4}) \right) \\ u_y(x) = \frac{P}{6\bar{E}I} \left(3\bar{\nu}y^2(L - x) + (4 + 5\bar{\nu})\frac{D^2x}{4} + (3L - x)x^2 \right) \end{cases} \quad (58)$$

³⁹⁰ where I is the beam's moment of inertia, \bar{E} and $\bar{\nu}$ are the material parameters
³⁹¹ for plane strain hypothesis, they can be expressed by:

$$I = \frac{D^3}{12}, \quad \bar{E} = \frac{E}{1 - \nu^2}, \quad \bar{\nu} = \frac{\nu}{1 - \nu} \quad (59)$$

³⁹² And correspondingly, the stress components are evaluated by

$$\begin{cases} \sigma_{xx} = -\frac{P(L - x)y}{I} \\ \sigma_{yy} = 0 \\ \sigma_{xy} = \frac{P}{2I}(\frac{D^2}{4} - y^2) \end{cases} \quad (60)$$

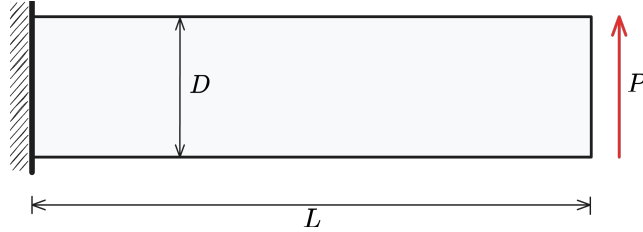


Figure 11: Illustration of cantilever beam problem

³⁹³ In this problem, the Quad4 element with 16×4 , 32×8 , 64×16 , 128×32
³⁹⁴ grids, and Quad8 element with 8×2 , 16×4 , 32×8 , 64×16 grids are em-
³⁹⁵ ployed for displacement discretization. The pressure is discretized by linear and
³⁹⁶ quadratic meshfree approximations with 1.5 and 2.5 characterized support sizes
³⁹⁷ respectively. The strain and pressure errors with respect to pressure nodes n_p
³⁹⁸ are displayed in Figure 12, where, to avoid the interpolation error, the pres-
³⁹⁹ sure nodes are uniformly distributed independent with displacement nodes by
⁴⁰⁰ the same way in Section 4.2. The vertical dashed lines stand for the stabilized
⁴⁰¹ number n_s . The figure implies that the Quad8 shows better performance than
⁴⁰² Quad4, since the Quad8's strain results are stable no matter the constraint ratio
⁴⁰³ is in the optimal range or not. And the Quad4's displacement errors increase
⁴⁰⁴ as soon as $n_p > n_s$. However, both Quad4's and Quad8's pressure errors imme-
⁴⁰⁵ diately increase while their constraint ratios are out of the optimal range, and
⁴⁰⁶ Quad8 still has better results than Quad4. Figure 13 shows the strain and pres-
⁴⁰⁷ sure error convergence comparisons with Quad4-RK, Quad8-RK with $r = n_d$,

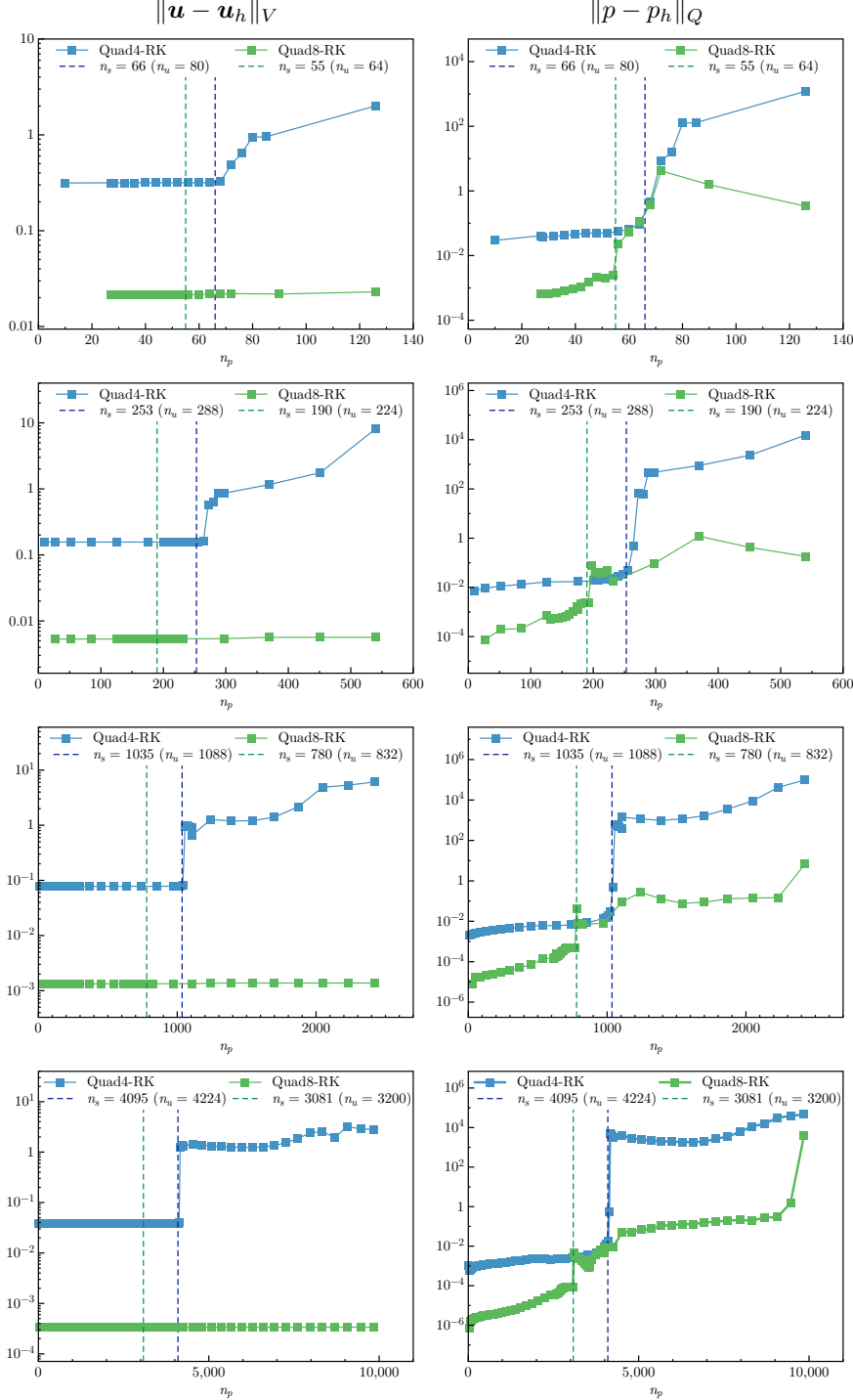


Figure 12: Strain and pressure errors vs. n_p for cantilever beam problem

408 $r = r_{opt}$ and traditional 4-node quadrilateral displacement element with 1-node
 409 piece constant pressure (Q4P1), 8-node quadrilateral displacement element with
 410 3-node piece linear pressure (Q8P3) for this cantilever beam problem, in which,
 411 except Quad8-RK($r = n_d$) for strain error, all formulations with the traditional
 412 constraint ratio of $r = n_d$ cannot ensure the optimal error convergence rates.
 413 The proposed mixed formulations with $r = r_{opt}$ and Q4P1, Q8P3 can maintain
 414 the optimal error convergence ratio, except the strain error of Quad8-RK is a
 415 little larger than that of Q8P3, the proposed approaches show good performance
 416 in accuracy.

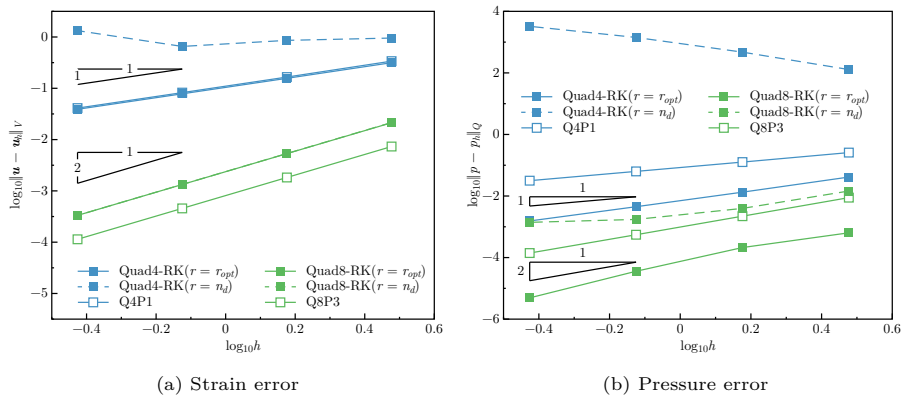


Figure 13: Error convergence study for cantilever beam problem

5.2. Plate with hole problem

418 Consider an infinite plate with a hole centered at the origin, as shown in
 419 Figure 14, and at the infinity towards the x -direction subjected to a uniform
 420 traction $T = 1000$. The geometric and material parameters for this problem are
 421 that the ratio of the hole $a = 1$, Young's modulus $E = 3 \times 10^6$, and Poisson's
 422 ratio $\nu = 0.5 - 10^{-8}$. The analytical solution of this problem refers to the
 423 Michell solution [60] as:

$$\begin{cases} u_x(\rho, \theta) = \frac{T a}{8\mu} \left(\frac{\rho}{a} (k+1) \cos \theta - \frac{2a^3}{\rho^3} \cos 3\theta + \frac{2a}{\rho} ((1+k) \cos \theta + \cos 3\theta) \right) \\ u_y(\rho, \theta) = \frac{T a}{8\mu} \left(\frac{\rho}{a} (k-3) \sin \theta - \frac{2a^3}{\rho^3} \sin 3\theta + \frac{2a}{\rho} ((1-k) \sin \theta + \sin 3\theta) \right) \end{cases} \quad (61)$$

424 in which $k = \frac{3-\nu}{1+\nu}$, $\mu = \frac{E}{2(1+\nu)}$. And the stress components are given by:

$$\begin{cases} \sigma_{xx} = T \left(1 - \frac{a^2}{\rho^2} \left(\frac{3}{2} \cos 2\theta + \cos 4\theta \right) + \frac{3a^4}{2\rho^4} \cos 4\theta \right) \\ \sigma_{yy} = -T \left(\frac{a^2}{\rho^2} \left(\frac{1}{2} \cos 2\theta - \cos 4\theta \right) + \frac{3a^4}{2\rho^4} \cos 4\theta \right) \\ \sigma_{xy} = -T \left(\frac{a^2}{\rho^2} \left(\frac{1}{2} \sin 2\theta + \sin 4\theta \right) - \frac{3a^4}{2\rho^4} \sin 4\theta \right) \end{cases} \quad (62)$$

425 According to the symmetry property of this problem, only a quarter model
 426 with length $b = 5$ is considered as shown in Figure 14. The displacement is
 427 discretized by 3-node and 6-node triangular elements with 81, 299, 1089, and
 428 4225 nodes. The corresponding linear and quadratic meshfree formulations are
 429 employed for pressure discretization, and the characterized support sizes are
 430 chosen as 1.5 and 2.5, respectively. Figure 15 studies the relationship between
 431 strain, pressure errors, and n_p , . Unlike the quadrilateral element case in Sec-
 432 tion 5.1, the quadratic Tri6-RK shows worse results while the constraint ratio is
 433 out of the optimal range. And Tri3-RK exhibits less sensitivity in strain error
 434 than Tri6-RK, but its error is increasing while n_p goes up. Both Tri3-RK and
 435 Tri6-RK with constraint ratios under the optimal range perform acceptably.
 436 The corresponding error convergence study is presented in Figure 16, the tradi-
 437 tional MINI element and 6-node triangular displacement element with 3-node
 438 triangular pressure element (T6P3) are employed for comparison. The results
 439 show that only Tri3-RK with $r = 2$ shows a comparable result with the optimal
 440 one with $r = r_{opt}$. The other formulations with the traditional constraint ratio
 441 show lower accuracy and error convergence rates.

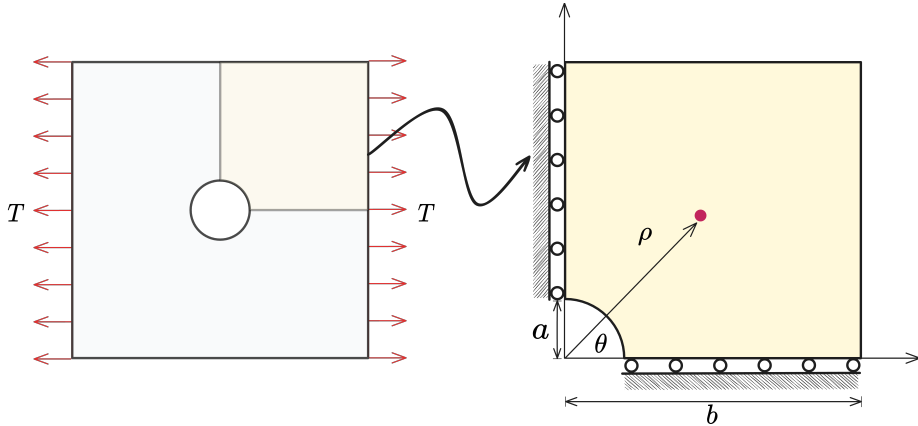


Figure 14: Illustration of plate with hole problem

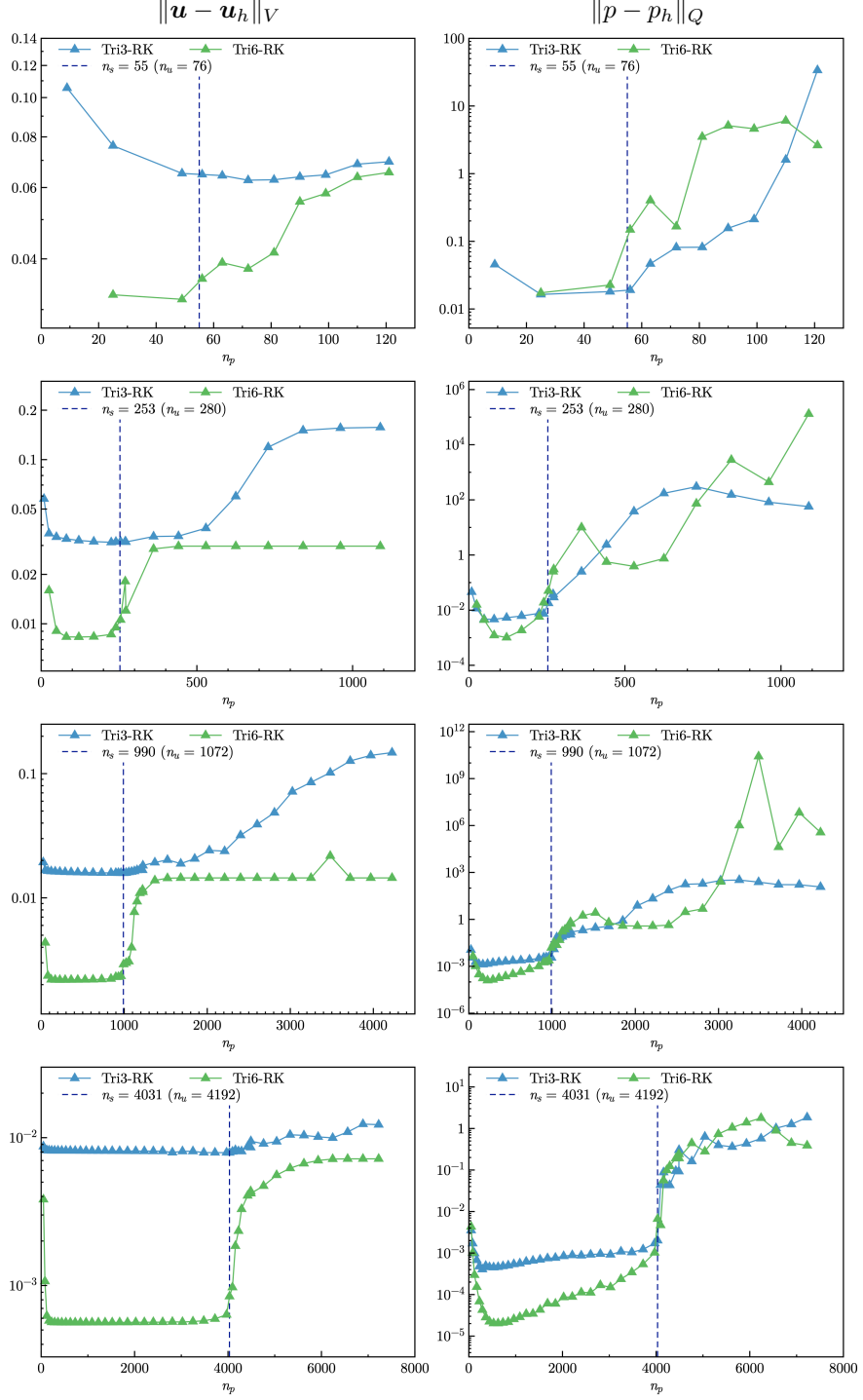


Figure 15: Strain and pressure errors vs. n_p for plate with hole problem

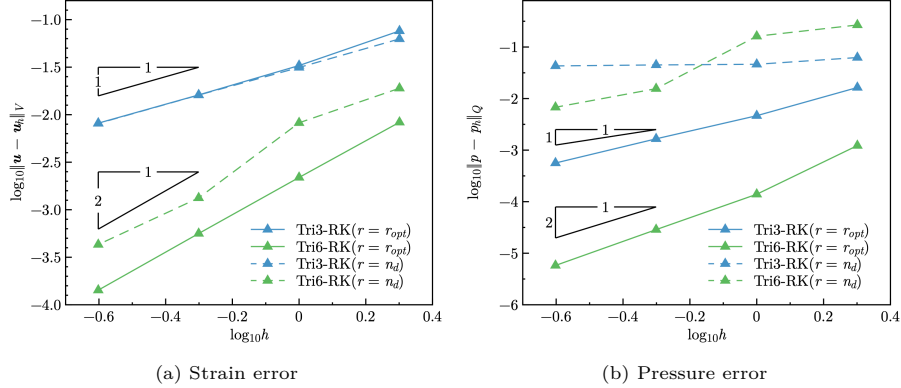


Figure 16: Error convergence study for plate with a hole problem

442 5.3. Cook membrane problem

The Cook membrane problem [12] is used herein for stability analysis of pressure. The geometry of this problem is shown in Figure 17, in which the left hand side is fixed and the right hand side subjects a concentrated force $P = 6.25$ in the y -direction. The material parameters are Young's modulus $E = 70.0$ and Poisson's ratio $\nu = 0.5 - 10^{-8}$.

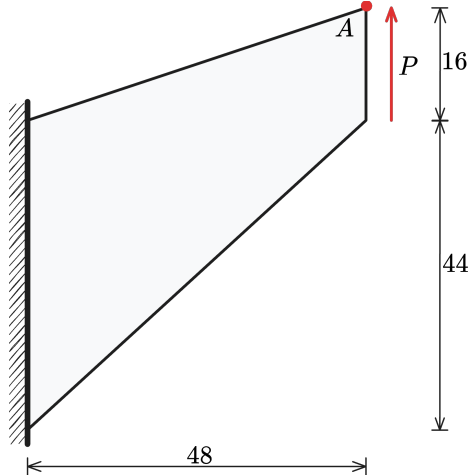


Figure 17: Illustration of Cook membrane problem

In this test, we focus on the pressure stability of 2D mixed FE–meshfree formulations. Figures 18–21 show the pressure contour plots for non-uniform Tri3–RK, Tri6–RK, Quad4–RK, and Quad8–RK formulations with $r = n_d$ and $r = r_{opt}$, respectively. The reproducing kernel meshfree approximations are employed for pressure discretization with characterized support sizes of 1.5 for the linear basis function and 2.5 for the quadratic basis function. The results

454 imply that the pressure contour plots with the optimal constraint ratio $r = r_{opt}$
 455 show a more stable and smooth pressure distribution compared to those with
 456 the traditional constraint ratio $r = n_d$.

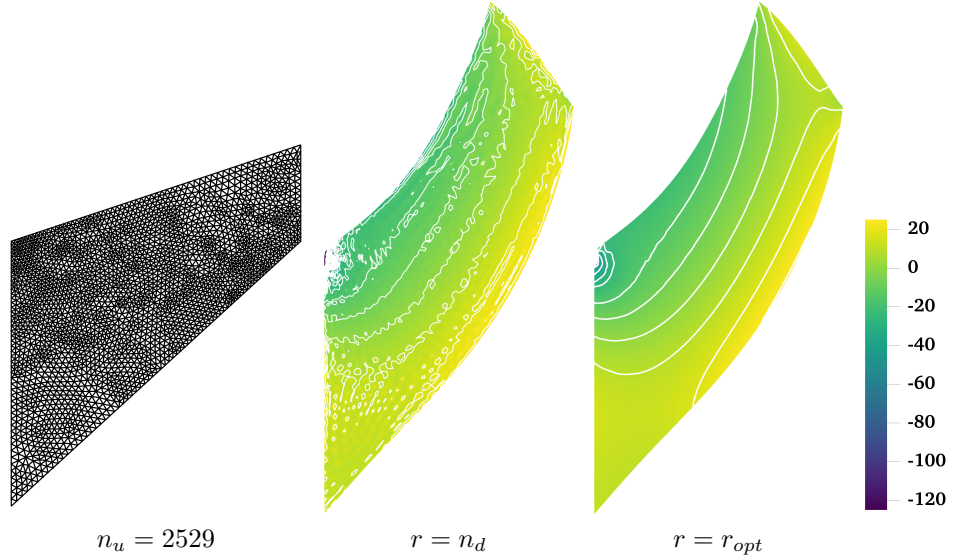


Figure 18: Pressure contour plots for Cook membrane problem using Tri3–RK

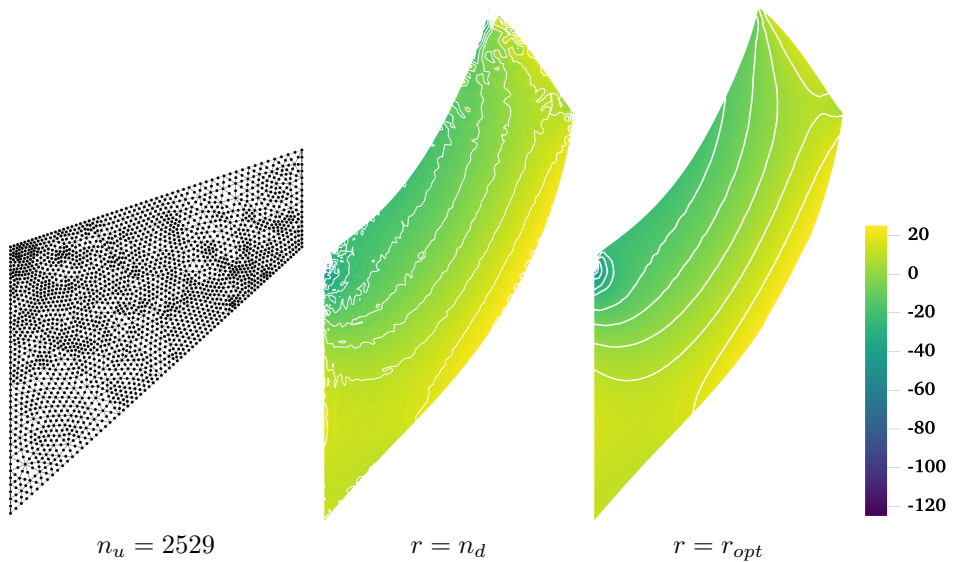


Figure 19: Comparison of pressure contour plots for Cook membrane problem using Tri6–RK

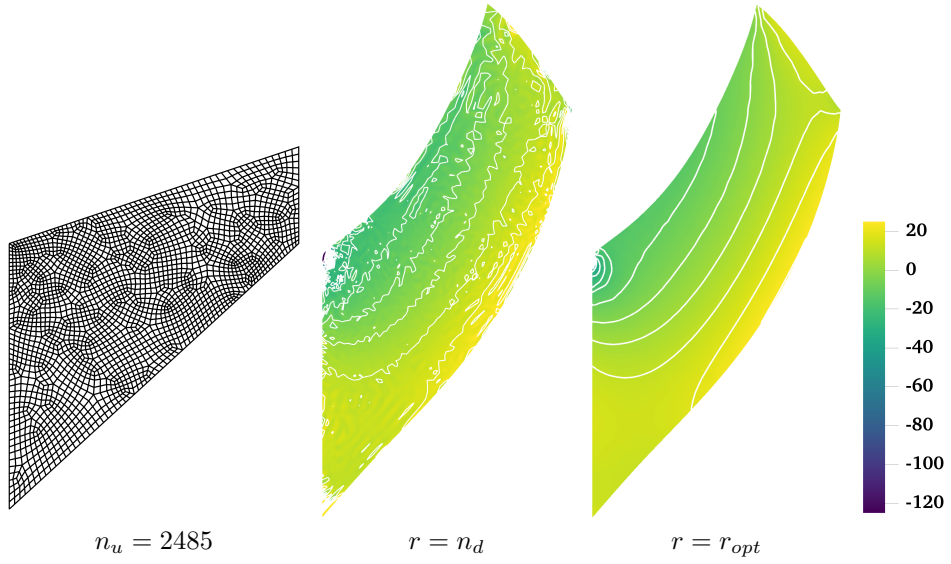


Figure 20: Comparison of pressure contour plots for Cook membrane problem using Quad4–RK

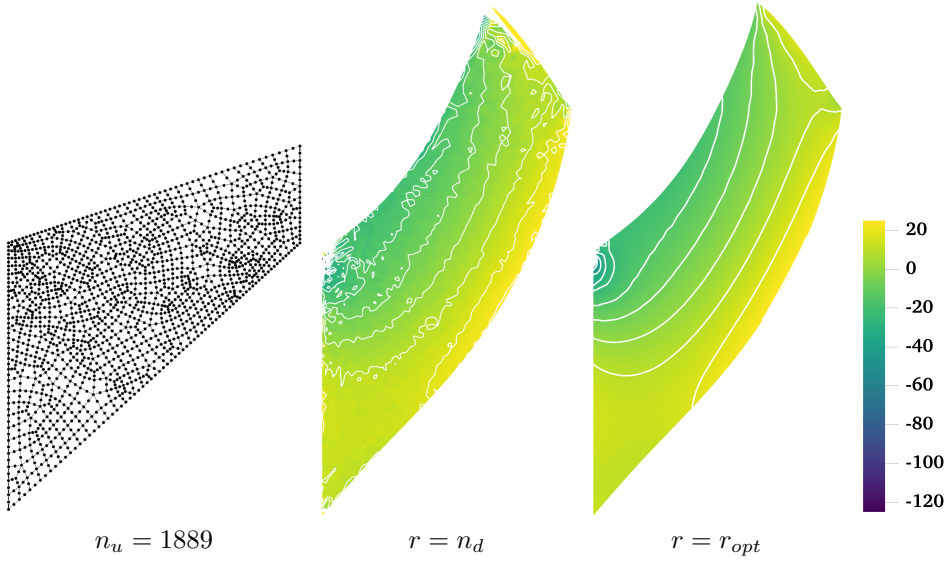


Figure 21: Comparison of pressure contour plots for Cook membrane problem using Quad8–RK

457 *5.4. Block under compression problem*

458 The incompressible block problem shown in Figure 22 is considered for test-
459 ing 3D mixed formulations. The block’s dimensions are $2L \times 2L \times L$, $L = 1$. At

460 the center of the top surface of the block is applied a pressure load $P = 80.0$
 461 with the area of $L \times L$. Due to the symmetry of this problem, only a quarter
 462 model is considered. The Young's modulus and Poisson's ratio are set as
 463 $E = 240.56839$ and $\nu = 0.5 - 10^{-8}$, respectively.

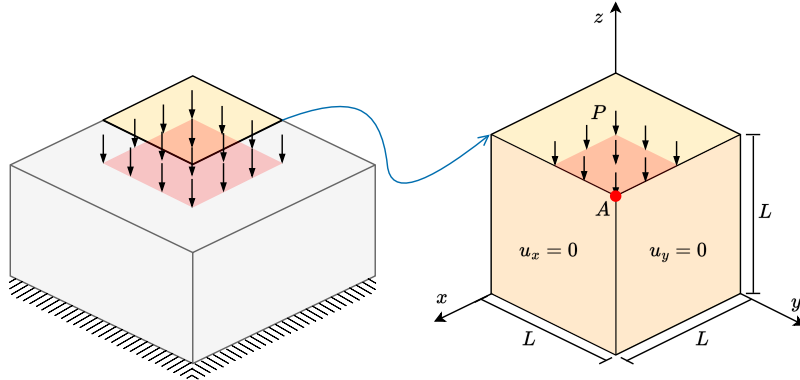


Figure 22: Illustration of block under compression problem

464 Figures study the pressure stability of 3D mixed FE-meshfree formulations,
 465 Tet4-RK and Hex8-RK, with non-uniform nodal distribution, while the pressure
 466 is discretized by linear meshfree approximations with a characterized support
 467 size of 1.5. The corresponding results also show the well performance of the
 468 proposed optimal constraint ratio $r = r_{opt}$. The mixed formulations with the
 469 traditional constraint ratio $r = n_d$ show comparable displacement results, but
 470 exhibit significant pressure instability.

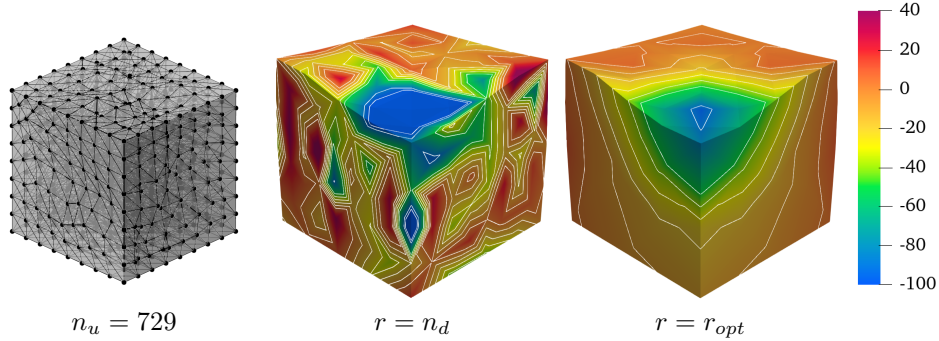


Figure 23: Comparison of pressure contour plots for block under compression problem using Tet4-RK

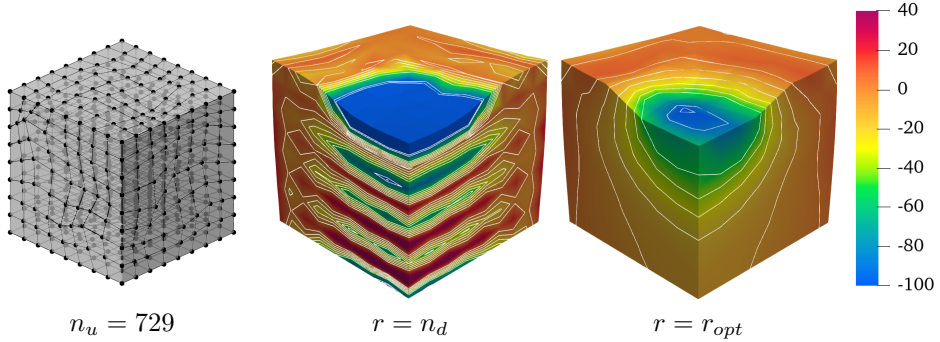


Figure 24: Comparison of pressure contour plots for block under compression problem using Hex8–RK

471 6. Conclusion

472 This paper proposes a novel optimal constraint ratio derived from the inf–sup
 473 condition to address volumetric locking. The optimal constraint ratio requires
 474 that, for a given number of displacement DOFs, the number of pressure DOFs
 475 should remain below a stabilized number determined by the proposed inf–sup
 476 value estimator. For well-posed nodal distribution, simply counting the dis-
 477 placement and pressure DOFs can determine whether the formulation satisfies
 478 the inf–sup condition. Compared to the traditional constraint ratio, the pro-
 479 posed ratio is theoretically grounded in the inf–sup condition and thus is more
 480 precise.

481 To implement this constraint ratio, a mixed finite element (FE) and meshfree
 482 formulation is developed. Displacements are discretized using 3-node and 6-node
 483 triangular elements, 4-node and 8-node quadrilateral elements in 2D, and 4-node
 484 tetrahedral and 8-node hexahedral elements in 3D. Correspondingly, linear and
 485 quadratic reproducing kernel meshfree approximations are used for pressure
 486 discretization. The reproducing kernel approximation equips globally smooth
 487 shape functions, allowing arbitrary pressure DOF placement without the limit
 488 of element.

489 Inf–sup tests for mixed FE–meshfree formulations with different constraint
 490 ratios verify the effectiveness of the proposed inf–sup value estimator. For effi-
 491 ciency and ease of implementation, the final nodal distribution scheme selects
 492 every other displacement node as a pressure node, ensuring the optimal con-
 493 straint ratio and satisfying the inf–sup condition.

494 A series of 2D and 3D incompressible elasticity examples demonstrate the
 495 effectiveness of the proposed mixed formulation. Results show that formulations
 496 with the optimal constraint ratio yield accurate displacement and pressure solu-
 497 tions. When the constraint ratio exceeds the optimal value, errors rise sharply
 498 to unacceptable levels, with the 8-node quadrilateral element being the only
 499 exception that maintains good displacement accuracy. Error convergence stud-
 500 ies and pressure contour plots further confirm that mixed formulations with

501 the optimal constraint ratio achieve optimal convergence rates and effectively
502 suppress pressure oscillations.

503 **Acknowledgment**

504 The support of this work by the National Natural Science Foundation of
505 China (12102138) and the Fundamental Research Funds of Central Universities
506 (ZQN-1014) is gratefully acknowledged.

507 **References**

- 508 [1] F. Brezzi, M. Fortin, Mixed and Hybrid Finite Element Methods, Vol. 15 of
509 Springer Series in Computational Mathematics, Springer, New York, NY,
510 1991.
- 511 [2] T. J. Hughes, The Finite Element Method: Linear Static and Dynamic
512 Finite Element Analysis, Prentice Hall, New Jersey, 2000.
- 513 [3] I. Babuška, R. Narasimhan, The Babuška-Brezzi condition and the patch
514 test: An example, Computer Methods in Applied Mechanics and Engineering 140 (1-2) (1997) 183–199.
- 515 [4] K. J. Bathe, Finite Element Procedures, Prentice Hall, Englewood Cliffs,
516 New Jersey, 1996.
- 517 [5] D. S. Malkus, Eigenproblems associated with the discrete LBB condition for
518 incompressible finite elements, International Journal of Engineering Science
519 19 (10) (1981) 1299–1310.
- 520 [6] D. Chapelle, K. J. Bathe, The inf-sup test, Computers & Structures 47 (4)
521 (1993) 537–545.
- 522 [7] F. Brezzi, K. J. Bathe, Studies of finite element procedures the inf-sup
523 condition equivalent forms and applications.
- 524 [8] D. Gallistl, Rayleigh-Ritz approximation of the inf-sup constant for the
525 divergence, Mathematics of Computation 88 (315) (2019) 73–89.
- 526 [9] P. Hood, C. Taylor, Navier-Stokes equations using mixed interpolation,
527 Finite element methods in flow problems (1974) 121–132.
- 528 [10] D. S. Malkus, T. J. Hughes, Mixed finite element methods - Reduced and
529 selective integration techniques: A unification of concepts, Computer Meth-
530 ods in Applied Mechanics and Engineering 15 (1) (1978) 63–81.
- 531 [11] T. Shilt, R. Deshmukh, J. J. McNamara, P. J. O’Hara, Solution of nearly
532 incompressible field problems using a generalized finite element approach,
533 Computer Methods in Applied Mechanics and Engineering 368 (2020)
534 113165.
- 535

- 536 [12] J. C. Simo, M. S. Rifai, A class of mixed assumed strain methods and
 537 the method of incompatible modes, International Journal for Numerical
 538 Methods in Engineering 29 (8) (1990) 1595–1638.
- 539 [13] M. Broccardo, M. Micheloni, P. Krysl, Assumed-deformation gradient finite
 540 elements with nodal integration for nearly incompressible large deformation
 541 analysis, International Journal for Numerical Methods in Engineering 78 (9)
 542 (2009) 1113–1134.
- 543 [14] W. M. Coombs, T. J. Charlton, M. Cortis, C. E. Augarde, Overcoming vol-
 544 umetric locking in material point methods, Computer Methods in Applied
 545 Mechanics and Engineering 333 (2018) 1–21.
- 546 [15] S. Saloustros, M. Cervera, S. Kim, M. Chiumenti, Accurate and locking-free
 547 analysis of beams, plates and shells using solid elements, Computational
 548 Mechanics 67 (2021) 883–914.
- 549 [16] J. Simo, R. Taylor, K. Pister, Variational and projection methods for the
 550 volume constraint in finite deformation elasto-plasticity, Computer Meth-
 551 ods in Applied Mechanics and Engineering 51 (1-3) (1985) 177–208.
- 552 [17] C. R. Dohrmann, P. B. Bochev, A stabilized finite element method for the
 553 Stokes problem based on polynomial pressure projections, International
 554 Journal for Numerical Methods in Fluids 46 (2) (2004) 183–201.
- 555 [18] A. Valverde-González, J. Reinoso, B. Dortdivanlioglu, M. Paggi, Locking
 556 treatment of penalty-based gradient-enhanced damage formulation for fail-
 557 ure of compressible and nearly incompressible hyperelastic materials, Com-
 558 putational Mechanics 72 (2023) 635–662.
- 559 [19] B.-B. Xu, F. Peng, P. Wriggers, Stabilization-free virtual element method
 560 for finite strain applications, Computer Methods in Applied Mechanics and
 561 Engineering 417 (2023) 116555.
- 562 [20] F. S. Liguori, A. Madeo, S. Marfia, G. Garcea, E. Sacco, A stabilization-
 563 free hybrid virtual element formulation for the accurate analysis of 2D
 564 elasto-plastic problems, Computer Methods in Applied Mechanics and En-
 565 gineering 431 (2024) 117281.
- 566 [21] R. Alves de Sousa, R. Natal Jorge, R. Fontes Valente, J. César de Sá, A new
 567 volumetric and shear locking-free 3D enhanced strain element, Engineering
 568 Computations 20 (7) (2003) 896–925.
- 569 [22] K.-J. Bathe, The inf-sup condition and its evaluation for mixed finite ele-
 570 ment methods, Computers & Structures 79 (2) (2001) 243–252.
- 571 [23] T. J. R. Hughes, Multiscale phenomena: Green's functions, the Dirichlet-
 572 to-Neumann formulation, subgrid scale models, bubbles and the origins of
 573 stabilized methods, Computer Methods in Applied Mechanics and Engi-
 574 neering 127 (1) (1995) 387–401.

- 575 [24] R. Rossi, R. Zorrilla, R. Codina, A stabilised displacement-volumetric
 576 strain formulation for nearly incompressible and anisotropic materials,
 577 Computer Methods in Applied Mechanics and Engineering 377 (2021)
 578 113701.
- 579 [25] E. Karabelas, M. A. F. Gsell, G. Haase, G. Plank, C. M. Augustin, An
 580 accurate, robust, and efficient finite element framework with applications to
 581 anisotropic, nearly and fully incompressible elasticity, Computer Methods
 582 in Applied Mechanics and Engineering 394 (2022) 114887.
- 583 [26] R. Codina, I. Castañar, J. Baiges, Finite element approximation of stabi-
 584 lized mixed models in finite strain hyperelasticity involving displacements
 585 and stresses and/or pressure—An overview of alternatives, International
 586 Journal for Numerical Methods in Engineering (2024) e7540.
- 587 [27] L. Moreno, R. Wuechner, A. Larese, A mixed stabilized MPM formula-
 588 tion for incompressible hyperelastic materials using Variational Subgrid-
 589 Scales, Computer Methods in Applied Mechanics and Engineering 435
 590 (2025) 117621.
- 591 [28] T. J. R. Hughes, L. P. Franca, M. Balestra, A new finite element formu-
 592 lation for computational fluid dynamics: V. Circumventing the babuška-
 593 brezzi condition: A stable Petrov-Galerkin formulation of the stokes prob-
 594 lem accommodating equal-order interpolations, Computer Methods in Ap-
 595 plied Mechanics and Engineering 59 (1) (1986) 85–99.
- 596 [29] A. N. Brooks, T. J. R. Hughes, Streamline upwind/Petrov-Galerkin formu-
 597 lations for convection dominated flows with particular emphasis on the in-
 598 compressible Navier-Stokes equations, Computer Methods in Applied Me-
 599 chanics and Engineering 32 (1) (1982) 199–259.
- 600 [30] L. He, L. Jing, M. Feng, New stabilized mixed finite element methods for
 601 two-field poroelasticity with low permeability, Applied Mathematics and
 602 Computation 494 (2025) 129285.
- 603 [31] D. N. Arnold, F. Brezzi, M. Fortin, A stable finite element for the Stokes
 604 equations, CALCOLO 21 (4) (1984) 337–344.
- 605 [32] F. Auricchio, L. Beirão da Veiga, C. Lovadina, A. Reali, A stability study of
 606 some mixed finite elements for large deformation elasticity problems, Com-
 607 puter Methods in Applied Mechanics and Engineering 194 (9-11) (2005)
 608 1075–1092.
- 609 [33] A. Quarteroni, A. Valli, Numerical Approximation of Partial Differen-
 610 tial Equations, Springer Series in Computational Mathematics, Springer,
 611 Berlin, 1994.
- 612 [34] M. Crouzeix, P. Raviart, Conforming and nonconforming finite ele-
 613 ment methods for solving the stationary Stokes equations I, Revue

- 614 fran aise d'automatique informatique recherche op ationnelle. Math matique 7 (R3) (1973) 33–75.
 615
- 616 [35] U. Brink, E. Stein, On some mixed finite element methods for incompressible and nearly incompressible finite elasticity, Computational Mechanics 19 (1) (1996) 105–119.
 617
- 619 [36] T. Belytschko, Y. Y. Lu, L. Gu, Element-free Galerkin methods, International Journal for Numerical Methods in Engineering 37 (2) (1994) 229–256.
 620
- 621 [37] W. K. Liu, S. Jun, Y. F. Zhang, Reproducing kernel particle methods, International Journal for Numerical Methods in Fluids 20 (8-9) (1995) 1081–1106.
 622
- 624 [38] C. Rodriguez, T.-H. Huang, A variationally consistent reproducing kernel enhanced material point method and its applications to incompressible materials, Computational Mechanics (2023) 1–20.
 625
- 627 [39] S. W. Chi, J. S. Chen, H. Y. Hu, A weighted collocation on the strong form with mixed radial basis approximations for incompressible linear elasticity, Computational Mechanics 53 (2) (2014) 309–324.
 628
- 630 [40] L. Wang, Z. Qian, Y. Zhou, Y. Peng, A weighted meshfree collocation method for incompressible flows using radial basis functions, Journal of Computational Physics 401 (2020) 108964.
 631
- 633 [41] A. Ortiz-Bernardin, M. Puso, N. Sukumar, Improved robustness for nearly-incompressible large deformation meshfree simulations on Delaunay tessellations, Computer Methods in Applied Mechanics and Engineering 293 (2015) 348–374.
 634
- 637 [42] T. J. Hughes, J. A. Cottrell, Y. Bazilevs, Isogeometric analysis: CAD, finite elements, NURBS, exact geometry and mesh refinement, Computer Methods in Applied Mechanics and Engineering 194 (39-41) (2005) 4135–4195.
 638
- 641 [43] F. Auricchio, L. Beir o da Veiga, C. Lovadina, A. Reali, The importance of the exact satisfaction of the incompressibility constraint in nonlinear elasticity: Mixed FEMs versus NURBS-based approximations, Computer Methods in Applied Mechanics and Engineering 199 (5) (2010) 314–323.
 642
- 645 [44] A. Huerta, S. Fern andez-M ndez, Locking in the incompressible limit for the element-free Galerkin method, International Journal for Numerical Methods in Engineering 51 (11) (2001) 1361–1383.
 646
- 648 [45] J. Dolbow, T. Belytschko, Volumetric locking in the element free Galerkin method, International Journal for Numerical Methods in Engineering 46 (6) (1999) 925–942.
 649

- 651 [46] G. Moutsanidis, J. J. Koester, M. R. Tupek, J.-S. Chen, Y. Bazilevs, Treatment
 652 of near-incompressibility in meshfree and immersed-particle methods,
 653 *Computational Particle Mechanics* 7 (2) (2020) 309–327.
- 654 [47] G. Moutsanidis, W. Li, Y. Bazilevs, Reduced quadrature for FEM, IGA
 655 and meshfree methods, *Computer Methods in Applied Mechanics and En-*
 656 *gineering* 373 (2021) 113521.
- 657 [48] Z.-Y. Wang, Y.-F. Jin, Z.-Y. Yin, Y.-Z. Wang, Overcoming volumetric
 658 locking in stable node-based smoothed particle finite element method with
 659 cubic bubble function and selective integration, *International Journal for*
 660 *Numerical Methods in Engineering* 123 (24) (2022) 6148–6169.
- 661 [49] T. Elguedj, Y. Bazilevs, V. Calo, T. Hughes, B^- and F^- projection meth-
 662 ods for nearly incompressible linear and non-linear elasticity and plasticity
 663 using higher-order NURBS elements, *Computer Methods in Applied Me-*
 664 *chanics and Engineering* 197 (33-40) (2008) 2732–2762.
- 665 [50] J. S. Chen, S. Yoon, H. P. Wang, W. K. Liu, An improved reproducing
 666 kernel particle method for nearly incompressible finite elasticity, *Computer*
 667 *Methods in Applied Mechanics and Engineering* 181 (1) (2000) 117–145.
- 668 [51] C. M. Goh, P. M. F. Nielsen, M. P. Nash, A stabilised mixed mesh-
 669 free method for incompressible media: Application to linear elasticity and
 670 Stokes flow, *Computer Methods in Applied Mechanics and Engineering* 329
 671 (2018) 575–598.
- 672 [52] D. S. Bombarde, M. Agrawal, S. S. Gautam, A. Nandy, Hellinger–Reissner
 673 principle based stress–displacement formulation for three-dimensional iso-
 674 geometric analysis in linear elasticity, *Computer Methods in Applied Me-*
 675 *chanics and Engineering* 394 (2022) 114920.
- 676 [53] H. Casquero, M. Golestanian, Vanquishing volumetric locking in quadratic
 677 NURBS-based discretizations of nearly-incompressible linear elasticity:
 678 CAS elements, *Computational Mechanics* 73 (6) (2024) 1241–1252.
- 679 [54] A. Huerta, Y. Vidal, P. Villon, Pseudo-divergence-free element free
 680 Galerkin method for incompressible fluid flow, *Computer Methods in Ap-*
 681 *plied Mechanics and Engineering* 193 (12-14) (2004) 1119–1136.
- 682 [55] C. T. Wu, W. Hu, J. S. Chen, A meshfree-enriched finite element method
 683 for compressible and near-incompressible elasticity, *International Journal*
 684 *for Numerical Methods in Engineering* 90 (7) (2012) 882–914.
- 685 [56] T. Vu-Huu, C. Le-Thanh, H. Nguyen-Xuan, M. Abdel-Wahab, A high-
 686 order mixed polygonal finite element for incompressible Stokes flow analy-
 687 sis, *Computer Methods in Applied Mechanics and Engineering* 356 (2019)
 688 175–198.

- 689 [57] E. Stein, R. de Borst, T. J. R. Hughes (Eds.), Encyclopedia of Computational Mechanics, John Wiley, Chichester, West Sussex, 2004.
- 690
- 691 [58] I. Babuška, J. Osborn, Eigenvalue Problems, in: Handbook of Numerical Analysis, Vol. 2 of Finite Element Methods (Part 1), Elsevier, 1991, pp. 641–787.
- 692
- 693
- 694 [59] K. Yosida, Functional Analysis, 6th Edition, Classics in Mathematics, Springer-Verlag, Berlin Heidelberg, 1995.
- 695
- 696 [60] S. Timoshenko, J. Goodier, Theory of Elasticity, Engineering Mechanics Series, McGraw-Hill, 1969.
- 697